UNIVERSIDADE FEDERAL DE SANTA CATARINA

CENTRO TECNOLÓGICO

PROGRAMA DE PÓS-GRADUAÇÃO EM ENGENHARIA QUÍMICA

André Vinícius Andrade Bezerra

PDCs in silicon carbo-nitride and silicon nitride systems as electrode materials for supercapacitors applications

Florianópolis

2020

André Vinícius Andrade Bezerra

PDCs in silicon carbo-nitride and silicon nitride systems as electrode materials for supercapacitors applications

Florianópolis

2020

Ficha de identificação da obra

André Vinícius Andrade Bezerra

PDCs in silicon carbo-nitride and silicon nitride systems as electrode materials for supercapacitors applications

O presente trabalho em nível de doutorado foi avaliado e aprovado por banca examinadora composta pelos seguintes membros:

Prof. Fabiano Raupp Pereira, Dr.
Universidade do Extremo Sul Catarinense

Prof. Sergio Yesid Gomez Gonzalez, Dr.
Universidade Federal de Santa Catarina

Prof. José Alexandre Borges Valle, Dr.
Universidade Federal de Santa Catarina

Profa. Cintia Marangoni, Dra.
Universidade Federal de Santa Catarina

Certificamos que esta é a **versão original e final** do trabalho de conclusão que foi julgado adequado para obtenção do título de Doutor em Engenharia Química.

_____

Profa. Dra. Cíntia Soares
Coordenadora do Programa

_____

Prof. Dr. Ricardo Antonio Francisco Machado
Orientador

Florianópolis, 2020.

Este trabalho é dedicado a todos que de alguma forma contribuíram para que eu pudesse chegar até aqui.

RESUMO

O presente trabalho apresenta a obtenção de cerâmicas mesoporosas derivadas de polititanossilazanos e sua aplicação como material de eletrodo para aplicações como supercapacitores. Os polititanossilazanos foram sintetizados por reação entre o polissilazano HTT1800 e TDMAT, um precursor de Ti de baixo peso molecular. Os materiais sintetizados foram caracterizados e sua conversão polímero em cerâmica foi investigada em diferentes atmosferas de pirólise por FTIR, RMN e TGA. Ainda, o comportamento de cristalização e microestruturas das cerâmicas derivadas de polititanossilazanos foram investigados por DRX, Raman e MET. Os resultados mostraram a formação de fases cristalinas de TiN ocorridas na cerâmica amorfa do carbonitreto de silício em nitrogênio, enquanto o nitreto de silício foi formado sob amônia. Além disso, os polititanossilazanos sintetizados foram impregnados com sucesso usando um monólito de carvão ativado como modelo pelo método de nanocasting e foram posteriormente pirolisadas em diferentes atmosferas de amônia e nitrogênio. Caracterizações detalhadas foram investigadas por BET, DRX, Raman e SEM. Pode-se observar que todas as amostras exibiram excelentes valores de área superficial específica. Ademais, as cerâmicas mesoporosas apresentam caráter amorfo após tratamento térmico a 1400 °C, e apenas cristalização parcial principalmente de TiN é observada. Por fim, as cerâmicas mesoporosas SiCN e Si_3N_4 derivadas de polititanossilazanos foram testadas como eletrodos para aplicações em supercapacitores. O melhor desempenho eletroquímico foi obtido para amostras pirolisadas sob amônia com uma razão de Si:Ti de 2,5, sendo o mais alto desempenho já reportado para materiais de eletrodos baseados em PDCs não-óxidos em termos de capacitância específica. Os efeitos sinérgicos entre o monólito condutor de carvão ativado e a atividade catalítica das cerâmicas amorfas de Si_3N_4/SiCN com nanocristais de TiN são responsáveis pelo notável desempenho eletroquímico.

Palavras-chave: Cerâmicas derivadas de polímeros. Polititanossilazanos. Supercapacitores. Nanocompósitos eletroquímicos.

RESUMO EXPANDIDO

Introdução

Combustíveis fósseis como carvão, petróleo e gás natural têm desempenhado um papel significativo no fornecimento de energia. A energia produzida desta fonte de energia é altamente dependente, constituindo mais de 80% da energia total consumida no mundo. Os combustíveis fósseis podem ser extraídos e distribuídos a um custo relativamente baixo. No entanto, há uma crescente preocupação no esgotamento destes recursos, nas mudanças climáticas e na poluição do ambiente associada à combustão destas fontes energéticas. Deste modo, têm-se ganhado destaque na utilização de tecnologias limpas para geração de energia. A tecnologia de supercapacitores são uma das maiores tecnologias promissoras de energia limpa para o futuro. Dentre os componentes dos supercapacitores, o eletrodo é o material o mais importante. Portanto, a busca por materiais alternativos para eletrodos está sob constante investigação. Nas últimas décadas, as cerâmicas derivadas de polímeros (PDCs) baseadas em Si receberam uma atenção crescente no quadro de sistemas de armazenamento de energia devido à sua resistência química superior combinada com sua versatilidade de fabricação. No entanto, poucos artigos relataram o uso de PDC como material de eletrodo para supercapacitores. Até o momento, a maioria das publicações existentes relacionadas ao desempenho eletroquímico de eletrodos para supercapacitores utilizando PDCs se baseou em cerâmicas de SiOC.

Objetivos

Este trabalho tem como objetivo o desenvolvimento de cerâmicas micro/mesoporosas derivadas de polititanossilazanos e sua aplicação como material de eletrodo em supercapacitores.

Metodologia

Os polititanossilazanos foram sintetizados por reação entre o polissilazano HTT1800 e TDMAT, um precursor de Ti de baixo peso molecular. Os materiais sintetizados foram caracterizados por FTIR e RMN. Após o processo de síntese, os polititanossilazanos foram impregnados em monólitos de carvão ativado pela técnica de *nanocasting*. Duas estratégias foram empregadas para o tratamento térmico dos polímeros pré-cerâmicos e componentes mesoporosos. A primeira estratégia envolveu a pirólise sob fluxo nitrogênio. A segunda estratégia foi realizada usando amônia como atmosfera de pirólise. No entanto, para evitar a decomposição completa do monólito de carvão ativado na presença de amônia, o sistema foi primeiramente aquecido a 400 °C sob nitrogênio e, em seguida, o gás foi alterado para amônia. A conversão polímero em cerâmica foi investigada por FTIR, RMN e TGA. Ainda, o comportamento de cristalização e microestruturas das cerâmicas derivadas de polititanossilazanos foram investigados por DRX, Raman e MET. Por fim, as cerâmicas mesoporosas SiCN e Si_3N_4 derivadas de polititanosilazanos foram caracterizadas por BET, SEM, DRX, Raman e TEM e posteriormente testadas como eletrodos para aplicações em supercapacitores.

Resultados e Discussão

De acordo com os resultados de FTIR, observou-se que ao aumentar a quantidade de TDMAT na síntese (razão 2.5 para 1.0), nota-se uma diminuição significativa dos grupos Si-H e N-H do polissilazano, o que sugere que os dois grupos reativos estão

envolvidos na reação com o precursor de Ti. Análise de RMN indicaram que a síntese dos polititanossilazanos ocorre principalmente entre unidades Si-H e grupos $N(CH_3)_2$ presentes no TDMAT. A evolução estrutural dos polititanossilazanos durante a pirólise em amônia e nitrogênio foi estudada usando TGA, FTIR e RMN. Os resultados sugeriram a ocorrência de reações principalmente de acoplamento por desidrogenação e transaminação durante a pirólise. Após tratamento térmico em amônia, também foi observado a remoção de carbono livre. Os resultados mostraram a formação de fases cristalinas de TiC_xN_{1-y} ocorridas na cerâmica amorfa do carbonitreto de silício pirolisadas em nitrogênio, enquanto nanocristais de TiN foi formado e distribuído em uma matriz de nitreto de silício após tratamento térmico sob amônia. Também notou-se que o aumento da temperatura de pirólise promoveu o crescimento dos nanocristais. Além disso, os polititanossilazanos sintetizados foram impregnados com sucesso usando um monólito de carvão ativado pelo método de *nanocasting* e pirolisadas posteriormente em diferentes atmosferas de amônia e nitrogênio. Observou-se que todas as amostras apresentaram uma isoterma tipo II e IV de sorção. Além disso, as amostras também exibiram excelentes valores de área superficial específica. Ademais, as cerâmicas mesoporosas apresentam caráter amorfo após tratamento térmico a 1400 °C, e apenas cristalização parcial principalmente de TiN foi observada. Análises de DRX, Raman e MEV confirmaram a presença de carbono nas amostras pirolisadas sob amônia, demonstrando a retenção do molde. Provavelmente, isso se deve ao efeito dos nanocristais de TiN e das fases cerâmicas do Si_3N_4, que atuam como um revestimento que protege a superfície do molde. Como consequência, apenas o carbono livre é removido sob amônia. O melhor desempenho eletroquímico foi obtido para amostras pirolisadas sob amônia com uma razão de Si:Ti de 2.5, sendo o mais alto desempenho em termos de capacitância específica já reportado para materiais de eletrodo baseados em PDCs não-óxidos. Entretanto, a capacitância específica da cerâmica mesoporosa diminuiu com o aumento da taxa de varredura, o que sugere que a capacitância específica do eletrodo depende significativamente da taxa de varredura. A diminuição da capacitância especifica com o aumento da taxa de varredura pode ser atribuída ao acesso insuficiente dos íons na superfície do eletrodo.

Considerações Finais
Os resultados mostraram a que a síntese dos polititanossilazanos ocorre principalmente entre unidades Si-H e grupos $N(CH_3)_2$ presentes no TDMAT. Também sugere-se a ocorrência de reações de acoplamento por desidrogenação e transaminação durante a pirólise e, no caso de amônia, a remoção do carbono livre. Pós pirolisados em nitrogênio formaram nanocristais de TiN embebida em uma matriz amorfa de SiCN enquanto para o tratamento térmico em amônia resultou em nanocompósitos de TiN em uma matriz cerâmica de Si_3N_4. Ainda, cerâmicas micro/mesoporosas foram obtidas após impregnação e subsequente tratamento térmico em nitrogênio e amônia. Os resultados de Raman e DRX mostraram um alto grau de desordem dos monólitos cerâmicos derivados de polímeros. Além disso, imagens de TEM confirmaram a presença de nanocristais e de estruturas amorfa e grafítica. As cerâmicas micro/mesoporosas derivadas de polititanossilazanos apresentaram características promissoras que possibilitam seu uso como eletrodos, obtendo os maiores valores de capacitância específica baseados em PDCs não-óxidos. Os efeitos sinérgicos entre o monólito condutor de carvão ativado com elevada área superficial e a atividade catalítica das cerâmicas amorfas de Si_3N_4/SiCN com nanocristais são os principais responsáveis pelo notável desempenho eletroquímico.

Palavras-chave: Cerâmicas derivadas de polímeros. Polititanossilazanos. Supercapacitores. Nanocompósitos eletroquímicos.

ABSTRACT

The current work presents the synthesis and characterization of mesoporous polytitanosilazanes derived ceramics and its application as electrode materials for supercapacitors applications. The polytitanosilazanes were synthesized by reaction between of polysilazane HTT1800 and TDMAT, a low molecular Ti precursor. The synthesized materials were characterized and their polymer to ceramic conversion were investigated with different pyrolysis atmospheres by FTIR, NMR and TGA. Furthermore, the crystallization behavior and microstructures of polytitanosilazanes derived ceramics were investigated by XRD, Raman and TEM. The results showed the formation of TiN crystalline phases occurred within the amorphous ceramic of silicon carbo-nitride in nitrogen, while silicon nitride was formed under ammonia. Furthermore, the as-synthesized polytitanosilazanes were successfully impregnated using an activated carbon monolith as template by nanocasting method and subsequently pyrolyzed different atmospheres of ammonia and nitrogen. Detailed characterizations were investigated by BET, XRD Raman and SEM. It can be observed that all samples exhibit excellent values of SSA. In addition, the mesoporous ceramics are amorphous up to 1400°C, and only partial crystallization mainly of TiN phases is observed. Finally, polytitanosilazanes derived SiCN and Si_3N_4 mesoporous ceramics were tested as electrodes for supercapacitors applications. The best electrochemical performance was obtained for samples pyrolyzed under ammonia with a Si:Ti ratio of 2.5, which is the highest performances reported for electrodes materials based on non-oxide PDCs in terms of specific capacitance. The synergistic effects between the conductive activated carbon monolith and the catalytic activity of amorphous Si_3N_4/SiCN ceramics with nanoscaled TiN are responsible for the remarkable electrochemical performance.

Keywords: Polymer derived ceramics. Polytitanosilazanes. Supercapacitors. Electrochemical nanocomposites.

LIST OF FIGURES

LIST OF TABLES

LIST OF ABBREVIATIONS

ACM	Activated carbon monolith
BET	Brunauer–Emmett–Teller
BJH	Barrett–Joyner–Halenda
CDC	Carbide derived ceramics
CO_2	Carbon dioxide
CV	Cyclic voltammetry
EDLC	Electrochemical double layer capacitor
EDX	Energy dispersive X-ray
fcc	face-centered cubic
FTIR	Fourier-transform Infrared
HRTEM	High-resolution transmission electron microscopy
LA	Longitudinal acoustic
LO	Longitudinal optic
MS	Mass spectrometry
NMP	N-methyl-2-pyrrolidone
NMR	Nuclear Magnetic Resonance
PDC	Polymer-derived ceramics
PVDF	Polyvinylidene fluoride
SAED	Selected Area Electron Diffraction
SEM	scanning electron microscopy
SiC	Silicon carbide
SiCN	Silicon carbo-nitride
Si_3N_4	Silicon nitride
SSA	Specific surface area
TA	Transverse acoustic
TiN	Titanium nitride
TO	Transverse optic
TDMAT	Tertakisdimethylaminotitanium
TEM	Transmission electron microscopy
TGA	Thermogravimetric analysis
XRD	X-Ray Diffraction

CONTENTS

1 INTRODUCTION

Population growth followed by the rapid development of emerging economies have strongly boosted the global energy demand in the past decades - with an obvious impact on the increase of carbon dioxide (CO_2) emissions in the atmosphere. Meeting this energy demand and reducing greenhouse gas emissions usually moves in opposite directions and is undoubtedly one of the greatest challenges of the 21st century (NEJAT et al., 2015).

Fossil fuels such as coal, oil and natural gas have played a significant role in energy supply. The energy produced from this energy source is highly dependent, constituting more than 80 % of the total energy consumed in the world (DEMIRBAS, 2009). Fossil fuels still remains as the main source of energy in our modern economy and can be obtained and distributed at relatively low cost. However, there is a growing concern about the resources depletion, climate change and environment pollution related to the combustion of these energy sources. Therefore, the transition to energy models based on environmentally friendly technologies is the natural solution to be sought in the next years (OMER, 2017).

Although great strides have been made in the context of green energy technologies, the bottleneck of its large-scale implementation relies on the development of more efficient electrochemical devices for energy conversion and storage. To achieve the appropriate requirements for the next generation of electrochemical devices it is crucial to develop advanced electrodes materials with a dramatic enhancement of their power density, catalytic activity and durability (OMER, 2017).

Supercapacitors is one of the greatest promising technologies of clean energy for the future. Among the components of supercapacitors, electrode material is the most important. Within this context, the development of new electrodes depends on a meticulous adjustment of its chemical composition and nanostructure. Currently, carbon is the most widely used electrode material for a wide range of applications in electrochemical processes, such as batteries, supercapacitors and fuel cells. Among its main advantages are their relatively low cost, easy processability (can be processed

in a variety of forms with controllable porosity) and high electrical conductivity. In contrast, its low corrosion resistance in harsh environments leads to a decreasing electrochemical performance, especially after the long-term high voltage cycles and high-temperature operations (MUKHERJEE; REN; SINGH, 2018; ZHANG et al., 2016).

Therefore, the search for alternative electrode materials are under constant investigation. In the past decades, Si-based polymer-derived ceramics (PDCs) have received an increased attention in the frame of energy storage systems in reason of their superior chemical resistance combining with their manufacturing versatility. However, up to now, only few papers have reported the use of PDC as an electrode material for supercapacitors. So far, most of the existing publications related to the electrochemical performance of electrodes for supercapacitors based on PDCs have been focused on SiOC ceramics (MUKHERJEE; REN; SINGH, 2018).

1.1   OBJECTIVES

1.1.1   Main Objective

The general objective of this work was to produce Ti modified SiCN and Si_3N_4 ceramics and to evaluate their electrochemical performance as electrode materials for supercapacitors.

1.1.2 Specific objectives

a) Modify a commercially available silazane by the reaction of preceramic polymer HTT1800 with a titanium containing precursor, named tertakisdimethylaminotitanium (TDMAT), by varying the Si:Ti ratio on the polytitanosilazanes formation;
b) Investigate the influence of pyrolysis temperature and atmosphere (ammonia or nitrogen) on the polymer-to-ceramic conversion and the ceramic phase formation of the synthesized polytitanosilazanes;
c) Produce mesoporous 3D structures of Ti modified $SiCN/Si_3N_4$ systems by nanocasting and investigate the influence of the process parameters on their morphology;

d) Evaluate the electrochemical performance Ti modified SiCN/Si_3N_4 ceramics as electrodes for supercapacitors applications.

2 LITERATURE REVIEW

2.1   ENERGY STORE SYSTEM

Energy storing devices represent one of the next-generation energy and are an essential part to handle the problems providing additional advantages to improve stability, power quality and reliability of the power supply source. In this way, scientific and technological challenges of energy storage become increasingly important in order to develop a novel, efficient, and low cost energy storage technology (MATHIS et al., 2019; PAYMAN; PIERFEDERICI; MEIBODY-TABAR, 2008).

Currently, the major types of energy storage devices are fuel cells, batteries, supercapacitors and capacitors. Each system is related to specific applications by energy and power requirements (KIM et al., 2015). The Ragone plot for different storage technologies is represented in Figure 1. The limits of the regions are determined by internal and/or leakage losses of the system for sufficiently high and low power (CHRISTEN; CARLEN, 2000).

Even though power density of supercapacitor is greater than batteries and fuel cells, it is considerably lower than conventional capacitors. On the other hand, they possess higher energy densities in storing huge amounts of energy than capacitors but lower than batteries and fuel cells (GONZÁLEZ et al., 2016). These key attributes make supercapacitors more attractive and versatile materials because they fill the gap between capacitors and batteries (KIM et al., 2015).

The Ragone plot also shows the discharge time of the devices in diagonal lines (Figure 1). It can be observed that batteries are more convenient for long periods, whereas capacitors and supercapacitors for short time applications (CHRISTEN; CARLEN, 2000; GONZÁLEZ et al., 2016).

Figure 1 – Ragone plot for different energy storage devices.
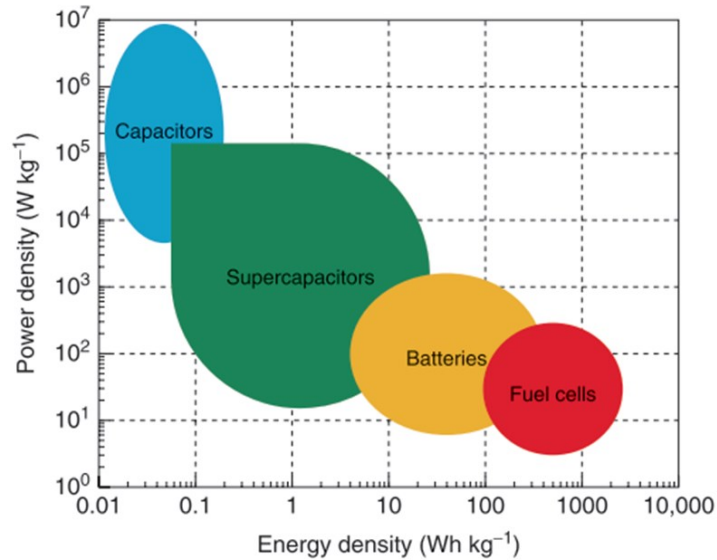
Source: Kim *et al.* (2015).

2.1.1 Batteries

Batteries store electricity in the form of chemical energy. Batteries are closed systems which consist of one or more electrochemical cells and each one involve an electrolyte together with a positive (cathode) and a negative electrode (anode) (Figure 2) (XIE *et al.*, 2016). A battery is charged by an internal chemical reaction under a potential applied to both electrodes. During discharge, electrochemical reactions occur at the two electrodes generating a flow of electrons through an external circuit. Currently, various types of batteries have been developed such as lead–acid, nickel cadmium, nickel metal hybrid, lithium–ion and sodium sulphur (XIE *et al.*, 2016; ZHAO *et al.*, 2015).

Carbon-based materials began to be commercially applied as anode in batteries in the early 1990s (ARMAND; TARASCON, 2008). Currently, the main anode commercially available in lithium batteries is graphite. Although it has some advantages, such as easy handling and low cost, there are some drawbacks of graphite anodes such as theoretical low electrode capacity (372 mA·h·g^{-1}), low kinetics at high load/discharge rates and insufficient performance use in portable electric and

electronic vehicles (GRACZYK-ZAJAC; FASEL; RIEDEL, 2011; GUOPING *et al.*, 2005; WU *et al., 2003*). In addition, graphite may suffers degradation in the exfoliation process due to the insertion of lithium ions in the graphene layers (GRACZYK-ZAJAC *et al.*, 2010).

Figure 2 – Schematic illustration of a lithium-ion battery.
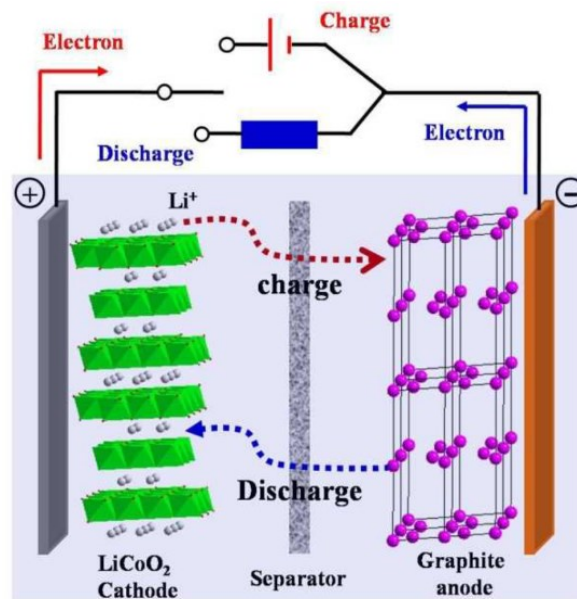
Source: Berckmans *et al*. (2017)

2.1.2 Fuel cells

Fuel cells are electrochemical devices that directly convert the chemical energy stored in fuels, such as hydrogen, into electrical energy. Fuel cells are classified according to the chemical characteristics of the electrolyte, which influences the type of catalysts as well as the chemical reactions involved. The type of electrolyte is a key factor for the type of fuel required and the temperature range (CARRETTE; FRIEDRICH; STIMMING, 2001; HAILE, 2003). Depending on the electrolyte applied as an ionic conductor, the efficiency will be different (KRAYTSBERG; EIN-ELI, 2014; WANG *et al.*, 2011). Table 1 shows the types of fuel cells and their main characteristics.

Table 1 – Some fuel cell types and main characteristics.

	Temperature (°C)	Fuel	Electrolyte	Mobile ion
AFC	<100	H_2	KOH aq.	OH^-
PEMFC	60-120	H_2, CH_3OH	Polymer	$(H_2O)_n\,H^+$
DMFC	60-120	CH_3OH	Polymer	H^+
PAFC	160-220	H_2	H_3PO_4	H^+
MCFC	600-800	Hydrocarbons, CO	$(Na,K)_2CO_3$	CO_3^{2-}
SOFC	700-1000	Hydrocarbons, CO	$(Zr,Y)_{O2-\delta}$	O^{2-}

AFC: alkali fuel cell; PEMFC: polymer electrolyte membrane; PAFC: phosphoric acid fuel cell; MCFC: molten carbonate fuel cell; SOFC: solid oxide fuel cell

Source: Carrete; Friedrich and Stimming (2001) and Haile (2003)

Hydrogen is the main fuel used in fuel cells and oxygen is usually employed as an oxidizer. The practice of hydrogen as a fuel is a promising alternative for energy purposes in relation to fossil fuels, as it is generated from clean sources, replacing toxic materials that are found in batteries, for example (DODDS *et al.*, 2015).

The PEM fuel cells are formed by an ion-conducting electrolyte, a cathode and an anode. The requirements of electrodes electrocatalyst in fuel cells depend on the type of cell and the nature of the fuel (DICKS, 2006). A schematic representation of the operating principle of this type of fuel cell is shown in Figure 3. In general, electrochemical reaction of hydrogen (fuel) occurs at the anode that produces protons and are conducted to the cathode by the electrolyte. The electrons released from the reaction migrate to the cathode by an electric charge, where they react with protons and oxygen, forming water (SHAO-HORN *et al.*, 2007).

Figure 3 – Schematic of a typical PEM fuel cell.
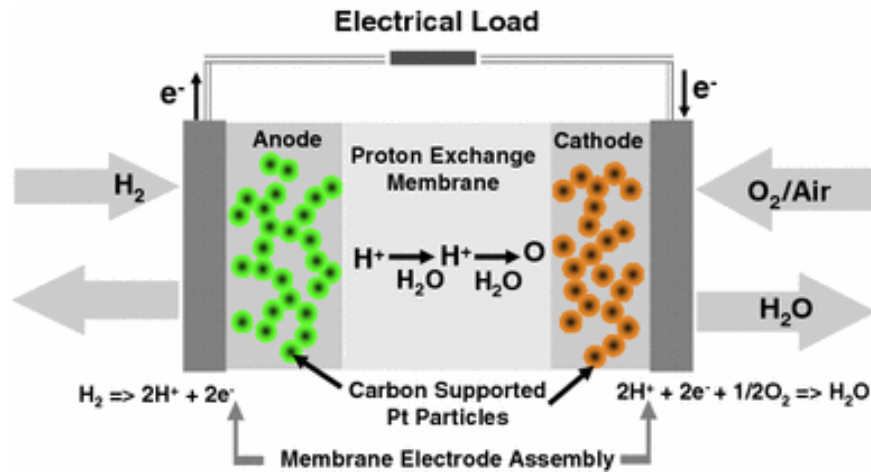
Source: Shao-Horn *et al*. (2007)

2.1.3 Supercapacitors

Supercapacitors are electrochemical devices used to store and supply energy at higher rates than those found in rechargeable batteries. Figure 4 illustrates the basic supercapacitor system that consists of two electrodes placed in an electrolyte solution with a separator (CAO; WEI, 2013). The separator isolates the two conducting electrodes electrically and only permits the ion mobility (WINTER; BRODD, 2004). Supercapacitors have been extensively used as energy storage devices for renewable energy systems. They have been used as electronic devices as Uninterruptible Power Supplies and volatile memory backups in PCs. Another typical supercapacitor application is its use in Hybrid Electric Vehicles, Electric Vehicles and Fuel Cell Vehicles. Besides that, supercapacitors is considered as a good candidate for applications in energy harvesting systems, solar arrays or wind turbines (LIBICH *et al*., 2018).

Figure 4 – Schematic representation of a supercapacitor.
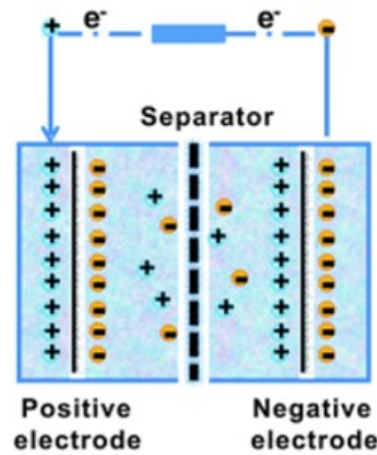
Source: Cao and Wei (2013)

Depending on the energy storage mechanism or cell configuration, supercapacitors can be classified as electrochemical double layer capacitor (EDLC), pseudocapacitors or hybrid supercapacitors (Figure 5). For EDLCs, the electric energy is stored on the interface of each electrode/electrolyte by application of a voltage to the system. The amount of stored energy is strongly dependent on the available electrode and electrolyte surface, the size of the ions, and the level of the electrolyte decomposition voltage. Among the EDLCs, high surface area carbon materials in their various forms, such as activated carbon, carbon nanotubes and graphene are examples of EDLCs electrodes (SAHAY; DWIVEDI, 2009).

Concerning pseudocapacitors, energy storage mechanism is based on redox reactions of faradic process which involves the transfer of charge between electrode and electrolyte. When the voltage is applied, reduction and oxidation processes occur on the electrode, which involve the passage of charge across the double layer, resulting in faradic current passing through the supercapacitor cell. As the energy stored is based on redox reactions, pseudocapactior behaviour is similar to batteries. Comparing to the EDLCs, the specific capacitance is higher in pseudocapacitors due to the redox reactions on the surface and in the bulk of electrode materials. Conductive

polymers and metal oxides are the most used electrode materials in pseudocapacitors (IRO; SUBRAMANI; DASH, 2016).

Hybrid supercapacitors are another class of supercapacitor. This system combines the non-Faradaic and Faradaic behaviour by coupling and EDLC or pseudocapacitor with a battery.

Depending on the nature of the electrode material supercapacitors can also be distinguished as symmetric and assymetric. In symmetric supercapacitors, the electrodes are fabricated of two identical material. In contrast, asymmetric supercapacitors can be fabricated with two different type of EDLC or pseudocapacitor, or one EDLC and one pseudocapacitor. Even the same electrodes but with different mass loadings/thickness are also classified as asymmetric supercapacitors (GONZÁLEZ *et al*., 2016)

Figure 5 – Classification of supercapacitors.
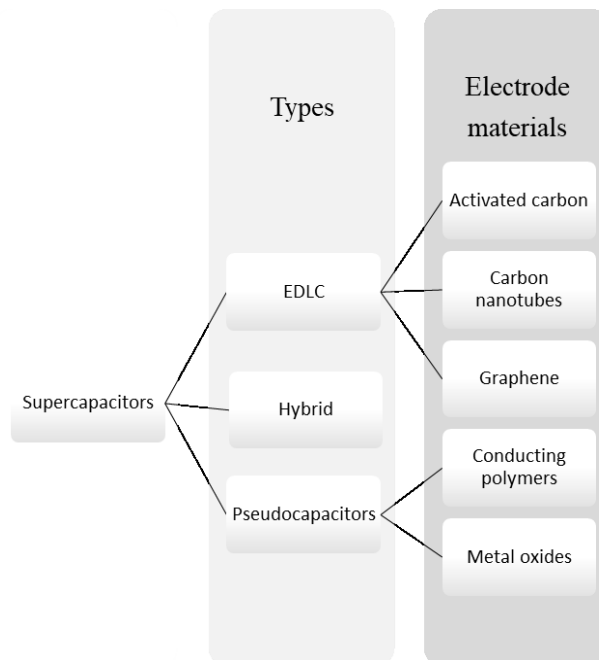
Source: Adapted from González *et al*. (2016)

2.2   POLYMER-DERIVED CERAMICS

Polymer-derived ceramics are polymers based on silicon chemistry that can be converted into a ceramic component by their pyrolysis in a controlled atmosphere (Figure 6) (LALE *et al*., 2018). Ainger and Herbert (1960), as well as Chantrell and

Popper (1965), described for the first time the production of non-oxide PDCs from molecular precursors. In the early 1970s, Verbeek, Winter and Mansmann report the first transformation of polyorganosilicon compounds (polysilazanes, polysiloxanes and polycarbosilanes) into ceramic materials (Si_3N_4/SiC fibers of small diameter). Thenceforward, a tremendous increase in the synthesis, technologies, and applications has greatly expanded the influence of PDC technique, and it continues today.

Figure 6 – The Polymer-Derived Ceramics route.
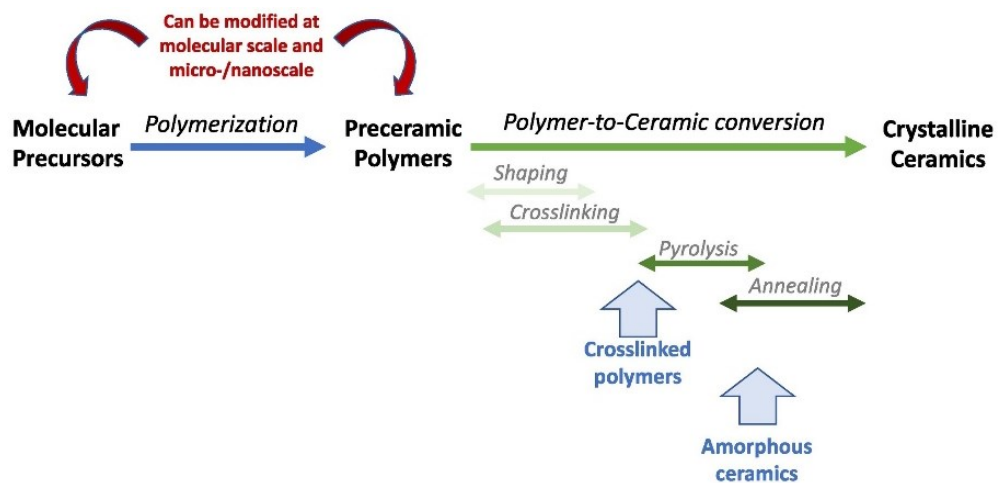
Source: Lale et al. (2018)

This class of materials is divided according to the components of the main chain. Figure 7 demonstrates in detail the organo-silicon polymer precursors and final ceramic structures. The main classes of Si-based polymers are polycarbosilanes (Si-C), polysiloxane (Si-O), polysilazanes (Si-N). The main systems of PDC includes not only secondary systems but also ternary like Si-O-C, Si-C-N, and quaternary systems as Si-B-O-C, Si-O-C-N, Si-Ti-C-N, among others.

Figure 7 – Typical classes of organosilicon polymers.
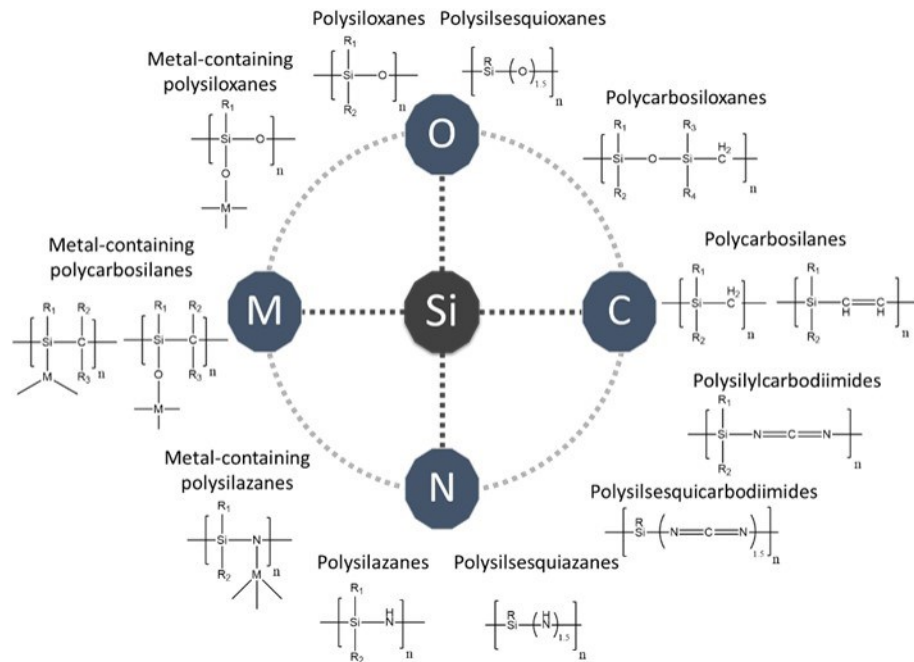
Source: Adapted from Colombo *et al.* (2010) and Mera *et al*. (2015)

Silicon-based pre-ceramic polymers provide the unique possibility of synthesizing new ceramic materials, which some of them are unable to be fabricated by conventional methods of ceramic production. They have the ability to adjust by chemical modification, being able to synthesize new multicomponent materials with remarkable properties (COLOMBO *et al*., 2010).

The route to obtain PDCs is an effective method to produce multicomponent and hybrid (organic-inorganic) materials by modification of precursors at molecular scale (molecular compounds), or at nano-/microscale (passive or active fillers). PDC route also allows the high versatility for the design of advanced ceramics with compositional and structural homogeneity. The main advantages of this treatment over traditional powder technology is the significant reduction of the processing temperature. In addition, the higher purity of the synthesized materials compared with those obtained by traditional powder technology is obtained (LALE *et al*., 2018).

PDC processing is composed of the following steps: i) Synthesis of the preceramic precursor; ii) shaping of the precursor; iii) Crosslinking of the precursor; iv)

pyrolysis of the polymer and subsequent conversion to ceramic. Among the silicon-based precursors, polysilazanes represent the preceramic polymer used in this study and will be further discussed in this literature review.

2.2.1 Synthesis and modification of the preceramic precursor

The synthesis of these ceramic precursors is usually carried out by the use of chlorosilanes, due to their commercial availability and low cost. Chlorosilanes enable their polymerization by means of chemical reactions of elimination, substitution or addition (COLOMBO *et al*., 2010).

The requirement that an organosilicon polymer should have to be appropriate for the production of PDC is high molecular weight to prevent any volatilization of low molecular oligomers during heat treatment. For shaping process, they should have desirable rheological properties and solubility. In addition, latent reactivity is required for curing and crosslinking step (FLORES *et al*., 2013; MERA *et al*., 2015).

As is well known, polysilazanes have been synthesized by aminolysis or ammonolysis reactions of the halosilanes (Figure 8). Co-ammonolysis of mixed chlorosilanes has been the most preferable simple method for the synthesis of silazanes. By varying the chlorosilazane monomers, the precursors can be organically modified by incorporation of suitable functional groups in the structure. Functional groups like hydrogen, aliphatic and aromatic groups are responsible for the solubility, thermal stability, electronic, optical and rheological properties of the polymer. The molecular structure and the type of preceramic polymer influence the composition, the phase distribution and microstructure of the final ceramic material (COLOMBO *et al*., 2010; DONG; ZHAO; XU, 2010; SONG; ZHAO; LU, 1994).

Figure 8 – General mechanism of aminolysis and ammonolysis reactions.
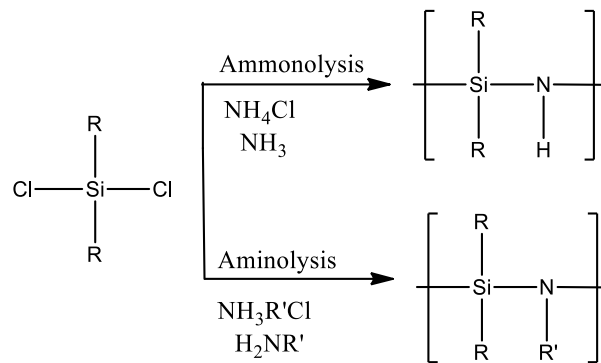
Source: Author

These preceramic polymers can be chemically modified with metal, mainly metal-containing polysiloxanes, polysilazanes and polycarbosilanes. Among them, it has been found that polysilazanes can be chemically modified by reactions with transition metal alkoxides and also with non-oxidic organometallics. Aluminium or group IV metal alkoxides (Ti, Zr, Hf) are the most commonly metals used to modify polysilazanes (MERA *et al.*, 2015).

2.2.2 Shaping of the precursor

The shaping of preceramic polymer is one of the main advantages of PDC route. Shaping technique can offer an innovative composition and microstructure, mainly in terms of design possibilities, but it poses new challenges in terms of process control. The shaping is related with the chemistry and degree of crosslinking, the type of bonds that link monomeric units and the nature of the functional groups attached to the polymer structure (FONBLANC et al., 2018). The high degree of crosslinking is required to increase the ceramic yield and avoid micro fracture during pyrolysis (SHAH; RAJ, 2002).

Different techniques of preceramic polymers have been use to allow polymer shaping and produce various complex structures/components. These shaping techniques could be impregnation/infiltration, tape casting, spraying, dip- or spin-coating, pressing, electrospinning, among others. The obtained shaped component is later subjected to thermal treatment to obtain the ceramic component (BERNARDO *et al.*, 2014; COLOMBO *et al.*, 2010). PDCs can be processed in different structural forms

such as powders, whiskers, foams, fibers, coating and porous materials (BIASETTO *et al*., 2008; BRINCKMANN *et al*., 2018; DICKS, 2006; MOURDIKOUDIS; LIZ-MARZÁN, 2013; TAMURA *et al*., 2013).

2.2.2.1 Design of mesoporous PDC via hard-template method

Hard-template approach, also called nanocasting, is one of the most common and established technique to design mesoporous components. The hard template-assisted PDC route have been widely developed to replicate the structure of a rigid material as a template/mold. In this method, a preceramic polymer is impregnated into the mesoporous structure of a template and then is converted to a ceramic by heat treatment with subsequent removal of the template (Figure 9). The template doesn't participate in the reactions during the conversion into ceramics (LALE *et al*., 2018).

Using this strategy, the pore morphology is obtained as a solid network being an inverse replica of the used template, as the walls of the template become the porous architecture of the PDC (BORCHARDT *et al*., 2012; LALE *et al*., 2018). The reproducibility of this technique is challenging mainly due to the volume shrinkage of precursors, the volatility of precursors or synthesis intermediates, and to the difficulty to preserve the ordering of the templates during thermal treatments in the nanocasting process (BORCHARDT *et al*., 2012).

Figure 9 – Hard-template method coupled with the PDC route.
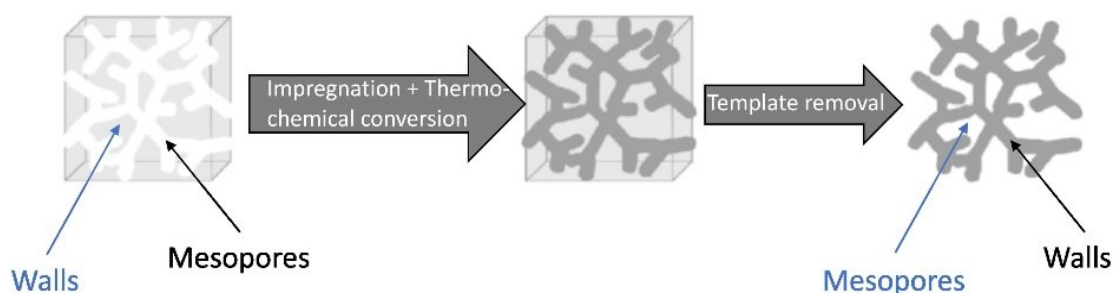
Source: Lale *et al*. (2018)

Several templates have been used on the production of mesoporous ceramics via PDC route. Among them, mesoporous carbon is the most used for preparing

mesoporous PDC. They are appropriate for energy storage systems, like supercapacitors, batteries and fuel cells. This is due to their regular pore structure and high specific surface area, in addition to the thermal and chemical stability (XIE *et al.*, 2016).

2.2.3 Crosslinking of the precursor

The crosslinking of preceramic polymer is an important aspect of the PDCs route. It occurs up to 400 °C and leads to infusible polymers, which retain their shape during pyrolysis. Crosslinking of preceramic polymers is accompanied by loss of low molecular weight components and fragmentation processes that increases the ceramic yield after pyrolysis (CHAVEZ *et al.*, 2011).

Crosslinking of polysilazanes can be performed thermally or using catalysts or peroxides. In general, the formation of thermally crosslinked products are arranged chiefly by hydrosilylation, dehydrocoupling, transaminations and vinyl group polymerisation reactions (KROKE *et al.*, 2002). The main reactions during crosslinking step are discussed foward.

2.2.3.1 Hydrosilylation

Hydrosilylation occurs in polysilazanes mainly at low temperatures and enables the formation of crosslinked products in the presence of functionalities such as vinyl groups ($Si-CH=CH_2$) and silyl (Si-H) groups, leading to the formation of Si–C linkages (Figure 10). These reaction can be induced with transition metals and/or metal-organic compounds as catalysts (IONESCU; KLEEBE; RIEDEL, 2012).

Figure 10 – General mechanism of hydrosilylation reactions.
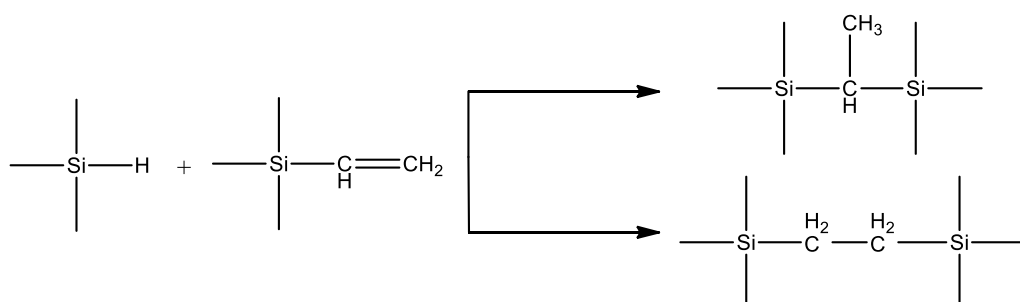
Source: Author

2.2.3.2 Dehydrocoupling

Dehydrogenative coupling reactions have a wide range of important applications in terms of both the main group element products formed and the H_2 gas released. Catalysts also promote Si–N and Si-Si coupling. The mechanism for this reaction is shown in Figure 11 (BELLINI *et al.*, 2016; FLORES *et al.*, 2013).

Figure 11 – General mechanism of Dehydrocoupling reactions.
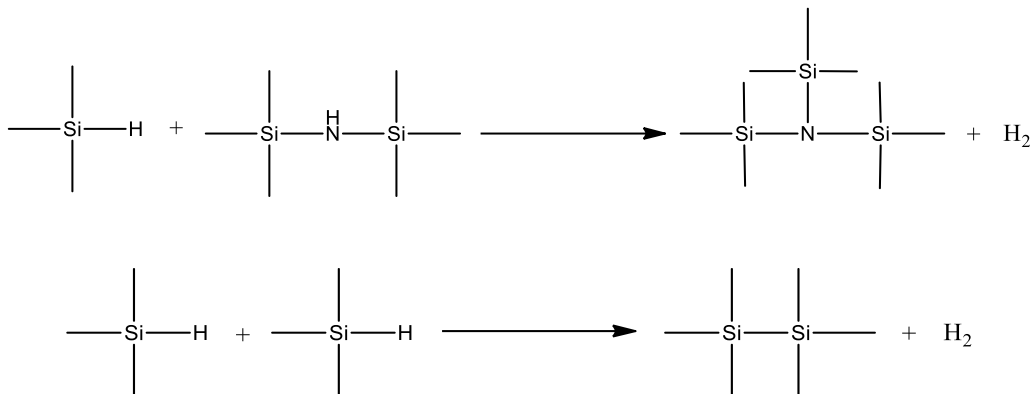
Source: Author

2.2.3.3 Transamination

Transamination reactions which lead to trisilylated nitrogen atoms, along with the release of ammonia (Figure 12) by thermal heating of oligosilazanes in a temperature range from about 200 to 400 °C. These reactions are related with amines, ammonia or oligomeric silazanes evolution, mass loss and decrease in nitrogen content of the final ceramic materials (CHAVEZ *et al.*, 2011; KROKE *et al.*, 2002).

Figure 12 – General mechanism of trasaminations reactions.
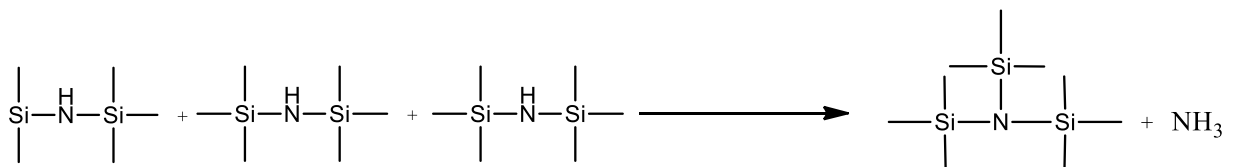
Source: Author

2.2.3.4 Vinyl polymerization

Polymerisation of the vinyl groups may also contribute to increase the crosslinking level. Vinyl polymerization processes lead to the transformation of sp^2 hybridized vinyl carbon atoms into sp^3 hybridized carbon (Figure 13) (KROKE *et al.*, 2002). Initiators such as AIBN or DCP have been used in order to generate radicals that initiate the vinyl polymerization (COAN *et al.*, 2015; RIBEIRO *et al.*, 2016).

Figure 13 – General mechanism of vinyl polymerization reactions.
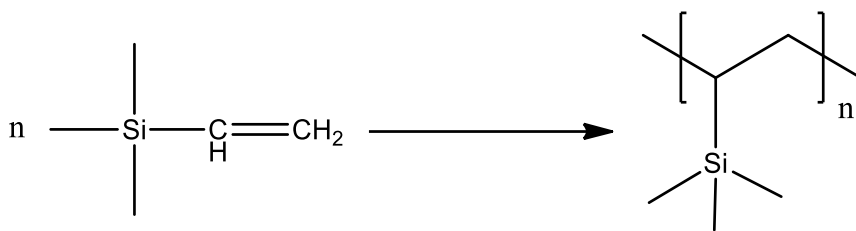
Source: Author

2.2.4 Pyrolysis

After shaping and crosslinking, the preceramic polymer is converted into a ceramic. The most common technique is pyrolysis using a furnace, but others nonconventional methods like microwave and laser have been reported (DANKO *et al.*, 2000; SUZUKI *et al.*, 1993). The chemical structure of the precursor has a strong influence in the crosslinking and ceramization processes. Moreover, even from the same preceramic polymer, different PDCs can be obtained by changing conditions for crosslinking and/or ceramization (temperature, heating rate, atmosphere) (DECKWERTH; RÜSSEL, 1994; BARROSO *et al.*, 2019)

Pyrolysis step can be performed in reactive (ammonia and air) or inert (nitrogen and argon) atmospheres. Pyrolysis occurs above 400 °C and is characterized to the polymer to ceramic transition and to the rearrangement and radical reactions resulted in cleavage of chemical bonds, with release of gaseous pyrolysis products. During this transformation, the density increase along with the mass loss which can cause high-volume shrinkage, as well cracks and pores formation (GREIL, 1995). The volume shrinkage can reach values around 40%, which is accompanied by the release of gaseous pyrolysis products that lead to the formation of pores and cracks. In

general, the conversion into ceramic is complete below 1100 °C (BARROSO *et al*., 2019; BORDIA; RAJ, 1985). Amorphous ceramics may be further annealed at high temperatures to form polycrystalline nanocomposites materials.

2.2.5 Applications of PDCs in Energy store systems

Among the several application of advanced ceramics fields, one of the most promising application is in energy store systems. PDCs are an interesting alternative for application as anode electrodes in batteries, as they have adequate electrochemical properties in the storage of lithium and sodium ions. In addition, they are lightweight and chemically inert to battery components, have high thermodynamic stability, open amorphous structure and processing flexibility (BHANDAVAT; PEI; SINGH, 2012). PDCs can have higher electrical properties than graphite (4000 mA·h·g^{-1}), which is the main anode used commercially available in Li-ion batteries, and have a more stable cycling behaviour even at high load/discharge rates (GRACZYK-ZAJAC; FASEL; RIEDEL, 2011; WILAMOWSKA; GRACZYK-ZAJAC; RIEDEL, 2013).

Carbon-rich SiCN and SiON ceramics have presented interesting electrochemical properties for the storage of Lithium ions (GRACZYK-ZAJAC *et al*., 2015). Ceramics with high carbon content using graphite and potato starch as a carbon precursor were reported. In both cases, the authors obtained a homogeneous material with potential use in lithium-ion batteries (GRACZYK-ZAJAC; FASEL; RIEDEL, 2011; WILAMOWSKA; GRACZYK-ZAJAC; RIEDEL, 2013). The presence of carbon for this application is essential to maintain its amorphous structure at elevated temperatures than low-carbon PDC analogue (MERA *et al*., 2009).

More recently, mesoporous PDC could be used as an excellent substitute beyond catalysis as electrodes in fuel and solar cells for example. The presence of mesoporous structure enhance the dispersion of the active phase and the accessibility of the electrolyte (LALE *et al*., 2016, 2018).

2.2.5.1 PDCs as electrodes for supercapacitors

PDCs received a lot of attention and exhibited versatile applications in many different fields. However, only few papers report the use of PDC to compose electrode materials for supercapacitors. So far, most existing publications related to the electrochemical performance of electrodes for supercapacitors based on PDCs have been focused on SiOC ceramics (MUKHERJEE; REN; SINGH, 2018). Table 2 summarizes some of the important results of using PDCs as electrodes for supercapacitors such as the preceramic polymer, polymer-derived ceramic, the pyrolysis of preceramic polymers, as well as the Specific surface area (SSA) and capacitance values.

Kolathodi and colleagues (2016) developed a layer-by-layer PDC-based on SiOC graphene composite with a specific capacitance of 75.72 F·g^{-1} at 6.7 A·g^{-1} and a capacitance retention of 56.13 % after 464 cycles. The electrodes were prepared mixing exfoliated graphene oxide (GO) and polysiloxane and then pyrolyzed at 800 °C in argon to produce free-standing SiOC–graphene composite papers (KOLATHODI *et al*., 2016). Also, Tolosa *et al.* (2016) prepared synthesized highly nanoporous fibers by electrospinning of a commercially available silicone resin. The fibers were prepared by chlorine gas treatment at 1200 °C. The fibers presented a high SSA of 3089 m^2·g^{-1}, specific capacitance of 135 F·g^{-1} at 10 mV·s^{-1} and a capacity retention of 63 % at current densities of 100 A·g^{-1}.

Similar values of specific capacitance and SSA were also observed by Yang *et al*. (2017). The authors obtained specific capacitance of 163 F·g^{-1} at a current density of 0.5 A·g^{-1} and a high specific surface area of 3122 m^2·g^{-1} from nonporous SiOC ceramic derived from pyrolysis of polysiloxane and sequentially etching with NaOH solution. Besides, Halim *et al*. (2017) surveyed the performance of low carbon ceramic-based SiOC coupled with an activated carbon electrode. SiOC ceramics was pyrolyzed at different temperature in argon atmosphere using silicon oil using as SiOC source. They found that the current production performance of hybrid ceramics exhibit a pseudocapacitive behaviour providing an energy density as high as 25 W·h·kg^{-1} with 98.7 % capacity retention over 40000 cycles (HALIM *et al*., 2017).

Table 2 – List of PDCs as electrodes for supercapacitors.

Preceramic polymer	PDC	Pyrolysis °C	SSA m²g⁻¹	Max. specific capacitance F g⁻¹	Reference
Silicone oil	SiOC AC	700-1000	2638	~70	Halim *et al*. (2017)
Poly(ureamethylvinyl)silazane	Si(B)CN– CNT- rGO	1000	-	269	David *et al*. (2016)
Polymethylphenylsilsesquioxane	SiOC-CDC	1200	3089	135	Tolosa *et al*. (2016)
Polymethylhydrosiloxane	SiOC (Activation with NaOH)	1200	3122	163	Yang *et al*. (2017)
Polymethyl(phenyl)siloxane	SiOC	1200-1600	71	149	Liqun *et al*. (2015)
Phenyltrimethoxysilane	SiO-CDC	700-1300	2000	110	Meier *et al*. (2014)
Tetravinyl-cyclotetrasiloxane	SiOC–rGO	800	-	76	Kolathodi *et al*. (2016)
Tetravinylcyclotetrasiloxane	SiOC-BN– rGO	1000	-	79	Abass *et al*. (2017)
Allylhydridopolycarbosilane	SiC-CDC	1000	2430	170	Korenblit *et al*. (2010)
Polymethylphenylsilsesquioxane	SiOC	1000	1798	333	Swain *et al*. (2019)

Source: Author

In another paper, Abass and co-authors (2017) produced a novel type of PDC composite based on SiOC embedded with varying wt % of boron nitride nanotubes and supported on reduced graphene oxide. The SiOC with 0.5 wt % boron nitride nanotubes electrode demonstrated the highest specific capacitance corresponding to 78.93 $F \cdot g^{-1}$ at 1 $A \cdot g^{-1}$ with a cyclic retention of 86 % after 185 cycles.

Polysiloxane-derived SiOC PDC have also been adopted as the carbide derived ceramics (CDC) precursors by adjusting pyrolysis conditions such as temperature, precursor kind, particle size, and dwelling time. Korenblit and others (2010) reported for the first time CDC material prepared using SiC precursor having ordered mesopores applying chlorination treatment. The authors exhibited a specific surface area up to 2430 $m^2 \cdot g^{-1}$ and a specific capacitance up to 170 $F \cdot g^{-1}$.

Meier and co-workers (2014) described the preparation of a novel silicon oxycarbide-derived carbons obtained by pyrolysis and chlorination of a polyphenylsilsesquioxane pre-ceramic precursor. The authors revealed that the carbon structure and the electronic behaviour can be controlled with the influence of pyrolysis and chlorination temperature. Chlorination at 700 and 1000 °C led to electrodes with high SSA of 2000 $m^2 \cdot g^{-1}$ and specific capacitances of up to 110 $F \cdot g^{-1}$.

Liqun *et al*. (2015) have reported CDC powders prepared from SiOC via chlorination with post treatment in ammonia using a commercially available polymethyl(phenyl)siloxane resin. High specific capacitance value of 148.7 $F \cdot g^{-1}$ with capacitance retention of up to 94.3 % after 2000 cycles at current densities of 1 $A \cdot g^{-1}$ was obtained (LIQUN *et al*., 2015). In another approach, polysiloxane polymer beads were prepared with different ratios of phenyl- and vinyltrimethoxysilane mixtures. These beads were subject to pyrolysis and obtained SiOC accompanied to chlorine gas treatment to form CDC. The specific capacitance of the best sample at low rates is 116 $F \cdot g^{-1}$ (at 5 $mA \cdot g^{-1}$) (KRÜNER *et al*., 2017). Recently, Swain and others reported the production of carbon hybrids by coating a preceramic polymer around a nano-template, followed by HF leaching. The authors obtained specific capacitance of 333 $F \cdot g^{-1}$ and a high specific surface area of 1798 $m^2 \cdot g^{-1}$ (SWAIN; PATI; BEHERA, 2019).

Furthermore, SiCN ceramic composites synthesized from preceramic polymers have been investigated. David *et al*. (2016) used preceramic polymers with multi-walled CNTs by chemical interfacing method. Samples were prepared using vacuum filtration of PDC-graphene oxide (GO) dispersion, followed by thermal reduction at 500 °C. Specific capacitance of 269 $F \cdot g^{-1}$ was obtained at scan rates of 5 $A \cdot s^{-1}$ for Si(B)CN–CNT–rGO.

In summary, Table 2 showed previous works of electrodes based on PDC for supercapacitors applications. In most of the literature data, SiOC ceramics have been employed as electrodes for supercapacitors. Moreover, as can be seen in Table 2, only

one study has reported the use of polysilazanes as preceramic polymer. In addition, papers which combine the metal-modified PDCs and their application in energy stored systems are very scarce in the literature. For this reason, based on the available literature, this work focuses on metal modification of silazanes, their structural evolution and application as electrodes for supercapacitors.

3 EXPERIMENTAL PROCEDURE

3.1   MATERIALS

The preceramic precursor used in this research was the oligosilazane HTT1800, commercially available as Durazane 1800 (Merck KGaA, Germany). Tetrakis-(dimethylamino)titanium (Ti[N(CH$_3$)$_2$]$_4$, TDMAT, 99.99%, Acros Organics) was used as Ti precursor. Toluene (99.85%, Extra Dry over Molecular Sieve, AcroSeal(R)), used as solvent, was obtained from Acros Organics. The activated carbon monolith (ACM), used on the nanocasting procedure, was acquired from ACS Materials. The ACM used for templating has a specific surface area of 953 m^2 g^{-1} and 5.2 nm of pore size. The chemical structure of the commercial oligosilazanes and Ti precursor are shown in Figure 14.

Figure 14 – Chemical structure of the commercial oligosilazanes and Ti precursor.

TDMAT   HTT1800
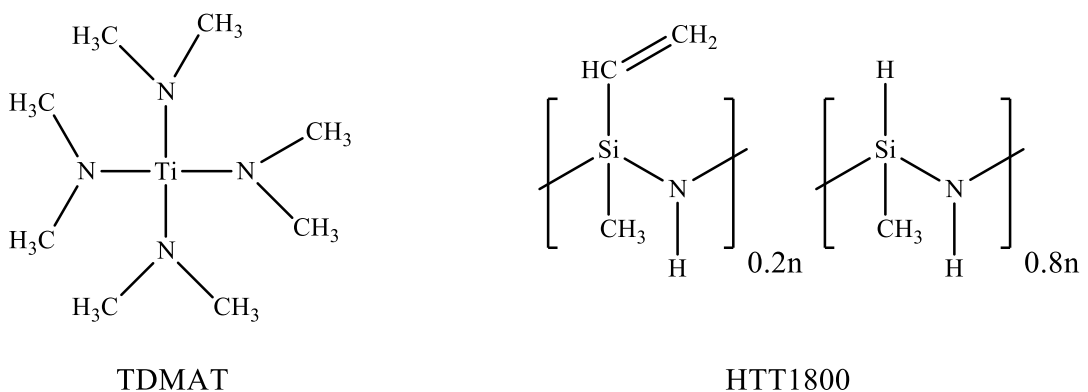
Source: Author

3.2   METHODOLOGY

The methodology for producing the mesoporous ceramics is described in Figure 15. The flowchart lists the major steps to produce the mesoporous ceramics and their application as supercapacitors. The details of each step will be introduced in the following sections.

Figure 15 – Schematic flowchart to produce Ti modified SiCN and Si_3N_4 mesoporous ceramics.
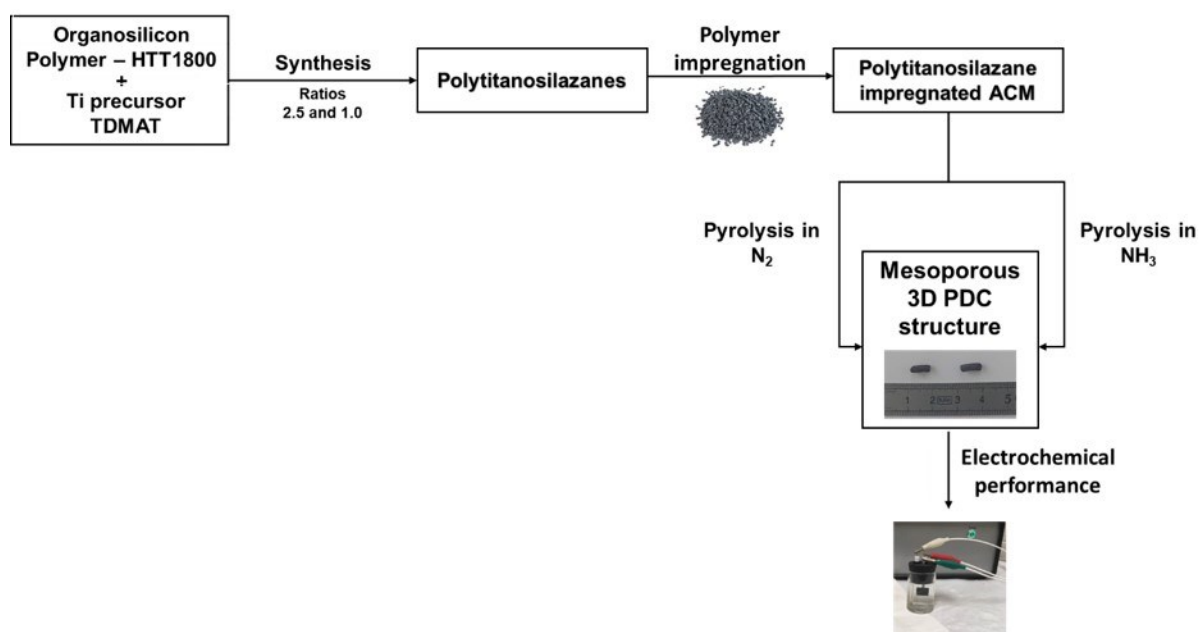
Source: Author

3.2.1 Polytitanosilazanes synthesis

Due to the high sensitivity of the inorganic polymer and Ti precursor to oxygen, mainly in relation to humidity, the reactions were conducted using standard Schlenk manipulations and vacuum/argon-line techniques, according to Shriver and Drezdzon procedures (1986). The argon atmosphere were purified by passing through successive columns of BTS-catalyst and P_2O_5.

Schlenk tubes were dried at 120 °C overnight before pumping under vacuum and filling them with argon for synthesis. The vacuum was applied for 30 min under the system to ensure the inert atmosphere.

The reactions were led in a flask under agitation in an oil bath, coupled with a reflux condenser, with an inlet system of gases and reagents. The commercially available Durazane (HTT1800) was used in the present study as SiCN source. HTT1800 has a nominal structure of $[Si(CH_2CH=CH_2)CH_2]_{0.2}[SiH_2CH_2]_{0.8}$. Manipulations of the polymer and Ti precursor was made inside an argon- filled glove box (Jacomex GP Campus).

Polytitanosilazanes were prepared by reaction of HTT1800 with two different amounts of TDMAT, using a Si:Ti molar ratio of 2.5 and 1.0, leading to polymers labeled NCHTiX, where X is the Si:Ti ratio. In a typical experiment, the as-received HTT1800 was dissolved in 150 mL of dry toluene at room temperature under an inert atmosphere. Then, TDMAT was added dropwise in the solution. As soon as the TDMAT was slowly added to the system, gaseous species were evolved and the solution changed the colour from yellow to black. The reaction was kept at room temperature for 3 h. Subsequently, the system was heated to 120 °C for 72 h. After this time, the system was cooled down to room temperature and then, the solvent was removed under reduced pressure. Depending on the Si:Ti ratio, the resulting sample range from a dark-black liquid to a dark solid powder. The final product was heated to 60 °C for 1 h under vacuum to remove any traces of toluene. To prevent samples oxidation, all the synthesized polytitanosilazanes were kept inside the glove box. This procedure was based on previously work reported on literature (BECHELANY *et al*., 2014; PROUST *et al*., 2016; SATO *et al*., 2006).

3.2.2 Nanocasting using ACM template

Impregnation of polytitanosilazanes was made by nanocasting method, using activated carbon monolith as template (LALE *et al*., 2016). Before impregnation, the ACM template was heat-treated at 650 °C for 10 h under air in vacuum in a tubular furnace to remove any residual of oxygen, moisture or dangling groups (-OH, -COOH), but without any structural modifications.

The treated monoliths were kept in to the glove box. A specific quantity of ACM were weighted and put in a Schelenk flask under dynamic vacuum for 30 min. After, using a mass polymer-to-template ratio of 1.4, the polytitanosilazanes were infiltrated under reduced pressure. In a dynamic vacuum, the system was sonicated for 24 h. After the absorption of the polytitanosilazanes into the pores of ACM, a wash step was performed using toluene. The excess of material was removed with a syringe under argon flow. Hence, the residual solvent was removed under low pressure at 30 °C for 1 h. The mesoporous samples were denoted as mNCHTiX, where X refers to Si:Ti ratio.

3.2.3 Pyrolysis of preceramic polymers and monoliths

Two thermal strategies were employed for the ceramization of the preceramic polymers and mesoporous components. The first strategy involved the pyrolysis under nitrogen at 1000 °C. The tube was pumped under vacuum and refilled with nitrogen (120 mL·min^{-1}) and subjected to a cycle of ramping of 5 °C·min^{-1} to 1000 °C, dwelling time of 2 h, and then cooling down to room temperature at 5 °C·min^{-1}. For mesoporous samples, the heating and cooling rate was 2 °C·min^{-1}.

The second strategy was done using ammonia as the pyrolysis atmosphere. To avoid the ACM complete decomposition in the presence of ammonia, the system is first heated at 400 °C under nitrogen, dwell time of 2 h and then the gas was changed to ammonia until 1000 °C. The heating hate was 5 and 2 °C·min^{-1} for powders and monoliths, respectively. Before pyrolysis, the tube was pumped under vacuum and refilled with nitrogen (120 mL·min^{-1}) (LALE *et al*., 2016).

The ceramic matrix and mesoporous components were annealed at temperatures up to 1500 °C under nitrogen. This procedure was conducted in a vertical furnace. Heat treatments using this furnace were done under nitrogen heating rate of 5 °C·min^{-1} up to the determined pyrolysis temperature for powders, remaining at this temperature for 2 h. For mesoporous samples, the heating and cooling rate was 2 °C·min^{-1} and dwelling of 2 h.

The pyrolyzed samples were denoted as NCHTiX@Y and mNCHTiX@Y for powders and mesoporous samples, respectively, where X refers to Si:Ti ratio and Y to pyrolysis temperature.

3.2.4 Application as supercapacitors

The resulting pyrolyzed samples (SA) were ground to powder and then mixed with carbon black (CB) and polyvinylidene fluoride (PVDF) binder in a wt% ratio SA:CB:PVDF of 80:10:10. A slurry of the composite material was prepared using N-methyl-2-pyrrolidone (NMP). The slurry was pasted uniformly on substrate of stainless steel sheet. After, the coatings were dried at 55 °C overnight in an oven.

Voltammograms were recorded with a solution prepared from Aq. 1M Na_2SO_4 as supporting electrolyte. An Ag/AgCl as reference electrode and platinum wire as contra electrode were used. Electrochemical properties were measured on a CHI660E (CH Instruments, Inc.) electrochemical workstation. Cyclic voltammetry (CV) measurements were performed in a potential window of 0 to 1.2 V at different scan rates of 10, 20, 50 and 100 $mV·s^{-1}$. The specific and areal capacitance of the tested electrodes was calculated using Eq. 1 and 2, respectively.

$$C_m = \frac{\int I.V \, d(v)}{\acute{v}.\Delta V.m}$$ (1)

$$C_a = \frac{\int I.V \, d(v)}{\acute{v}.\Delta V.a}$$ (2)

Where $\int I.V \, d(v)$ is the area enclosed by the CV curve, $\acute{v}$ is the scan rate in V/s, ΔV is the voltage window (range being scanned in V), m is the mass (in g) of the active material and a is the area of the active material exposed to the electrolyte (in cm^2).

3.2.5   Characterization

3.2.5.1   Fourier-transform Infrared Spectroscopy

The Fourier-transform Infrared Spectroscopy (FTIR) technique was used to observe bonds and functional groups of the polymer and the pyrolysis intermediates The samples were mixed with KBr inside the glove box and made into pellets. FTIR analysis was made in a Thermofischer Nicolet Nexus FT-IR machine, from 400 cm^{-1} to 4000 cm^{-1}. Collected data was analysed in OMNIC software.

3.2.5.2   Solid-state Nuclear Magnetic Resonance

Solid-state NMR were performed to investigate the structure of polymer-derived ceramics samples using a Bruker Avance 300MHz NMR equipment. Chemical shift values were referenced to tetramethylsilane for ^{29}Si.

3.2.5.3   Thermogravimetric analysis

Thermogravimetric Analysis (TGA) were carried out on a Netzsch thermal analysis equipment model STA 409/449 F3. The analyses were performed in polymer samples in order to investigate the polymer to ceramic conversion under nitrogen and ammonia atmosphere with flow rate of 40 mL·min^{-1}. The samples were heated up to 1400 °C with a heating rate of 5 °C·min^{-1}. The amount of sample used per analysis was approximately 30 mg.

3.2.5.4   X-Ray Diffraction

XRD analysis were performed in order to obtain information of the ceramics crystalline phases. The samples were analysed on a diffractometer Bruker D8 Advance Serie II, Bruker D8 Advance da Vinci, while EVA software aided on the analysis of the measured diffractograms. The samples were crushed and put on acrylic disks as a support during the analysis. The scan ranged from 5° and 90° in 2θ, with a 0.05° step and 1 second acquisition time for each stage.

The TiN nanocrystallites thickness were calculated from (1 1 1) peak using the following Scherrer equation (Eq. 3). Where β is the full-width at half the maximum intensity, λ is the X-ray wavelength, θ is the scanning angle and K is the shape factor.

$$L_c = \frac{K\lambda}{\beta\cos(\theta)} \tag{3}$$

3.2.5.5   Raman spectroscopy

Raman spectra were recorded on a Raman Renishaw 2000 microspectrometer using a power laser at 514.5 nm. The Spectra were recorded in the range of 100 e 3500 cm^{-1}. Before the measurements, the Raman spectrometers were calibrated with respect to the silicon peak (520.7 cm^{-1}). The I(D)/I(G) intensity ratio was

used to evaluate the carbon size using the formula reported by Ferrari and Robertson (Eq. 4).

$$\frac{I_D}{I_G} = C'\lambda L_a^2 \qquad (4)$$

Where La is the size of the carbon domains, and C' is a coefficient that depends on the laser wavelength (514.5 nm) and corresponds to 0.0055 Å^{-2}.

3.2.5.6 Transmission Electron Microscopy/Selected Area Electron Diffraction

Transmission Electron Microscopy (TEM) analyses were performed using a JEM-1011 model and a Jeol 2010 device microscope. The voltage used in the sample visualization was 100 kV. The samples were crushed, suspended in distillate water and deposited one drop on the Cu grid. After, they were dry at room temperature until complete water evaporation. SAED (Selected Area Electron Diffraction) was investigated to check the presence of amorphous and/or crystalline phases.

3.2.5.7 Scanning Electron Microscopy/Energy Dispersive X-ray Spectroscopy

The monoliths morphology after pyrolysis was analysed by Scanning Electron Microscopy (SEM) Jeol IT 300 LV. The Energy Dispersive X-ray Spectroscopy (EDX) for point areas was used to check the ceramic composition.

3.2.5.8 Brunauer–Emmett–Teller

The Brunauer–Emmett–Teller (BET) method was used to calculate the specific surface area of the mesoporous ceramic. The pore size distribution was calculated using Barrett–Joyner–Halenda (BJH) method. The total pore volumes were estimated from the amount adsorbed at a relative pressure of (P/P0) 0.99. The data was collected using a Micromeritics ASAP 2020 apparatus.

4 RESULTS AND DISCUSSION

4.1 SYNTHESIS OF THE POLYTITANOSILAZANES

The structures of the polysilazane and polytitanosilazanes were initially investigated by FTIR. The FTIR spectrum (Figure 16) of HTT1800 confirms the expected absorption bands of polyorganosilazanes (LÜCKE et al., 1997). The bands in the range of 2850-3050 cm^{-1} (stretching) and 1400-1250 cm^{-1} (bending) correspond to the C-H, CH_2 and CH_3 bonds. Vibration bands of Si-H and C-H bonds in $SiCH_3$ units are observed at 2126 and 1253 cm^{-1}, respectively. The bands at 3378 and 1155 cm^{-1} are attributed to the N-H bonds. Below 1000 cm^{-1}, it is observed an overlapping of the Si-C, Si-N, C-H, and C-C stretching modes, and cannot be assigned unambiguously.

Comparing the FTIR spectra of the NCHTi1.0 and NCHTi2.5 samples with pure HTT1800, new absorption bands appear at 2800-3000 cm^{-1} resulted from the C-H bond vibrations of TDMAT. In addition, the C-H stretching band derived from the TDMAT also is observed at wavenumber around 1360 and 1450 cm^{-1}. The band at 1280 cm^{-1} is assigned to the presence of N-C bonds in $N(CH_3)$ groups from TDMAT.

By increasing the amount of TDMAT in the synthesis reaction (from sample NCHTi2.5 to NCHTi1.0) a significant decrease of the Si-H and N-H groups from the silazane is noticed, which suggests that both reactive groups are involved in the reaction with the Ti precursor. Based on these results, two possible main pathways of the reaction between HTT1800 with TDMAT are proposed (BECHELANY et al., 2017; SATO et al., 2006; LALE et al., 2017). First $Ti[N(CH_3)_2]_4$ can react with N-H groups from HTT1800 to form Ti-N, as show in Eq. 5. The second reaction is between Si-H units and $N(CH_3)_2$ groups present in TDMAT, as shown in Eq. 6. The absence of a peak at 1620 cm^{-1} corresponding to vinyl groups presents in HTT1800 also confirms that TDMAT can act as catalyst during vinyl polymerization (Eq. 7) and/or hydrosilylation reactions (Eq. 8).

Figure 16 – FTIR spectra of polytitanosilazanes synthesized.

Source: Author

$$Si-NH + ((CH_3)_2)_4 \rightarrow Si-N-(N(CH_3)_2)_3 + H-N(CH_3)_2 \tag{5}$$

$$Si-H + (N(CH_3)_2)_4 \rightarrow Si-N(CH_3)-(Ti(N(CH_3)_2)_3) + CH_4 \tag{6}$$

$$n_2HC=CH\text{-}Si \rightarrow \text{-}(CH_2\text{-}CH_2)n\text{-}Si \tag{7}$$

$$Si\text{-}H + CH_2=CH\text{-}Si \rightarrow Si\text{-}CH_2\text{-}CH_2\text{-}Si \tag{8}$$
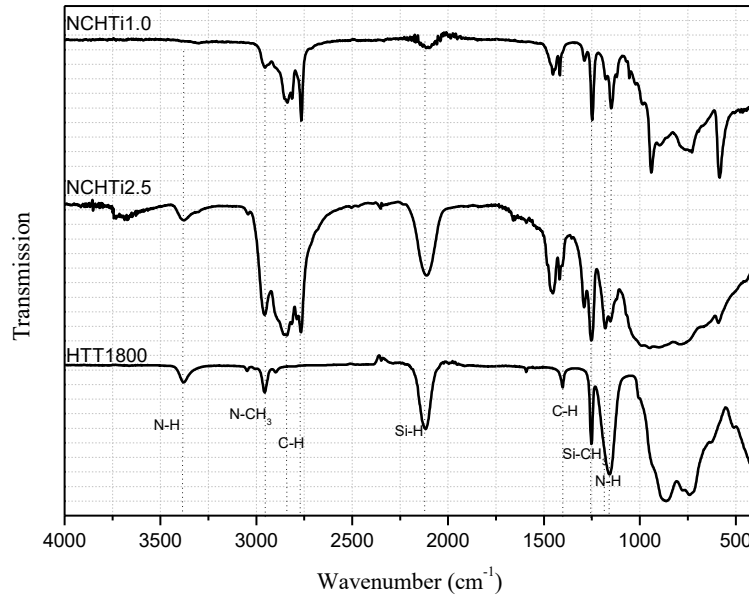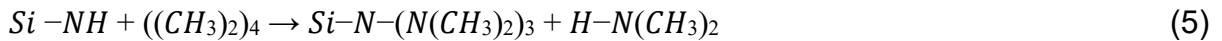
The elemental composition of the synthesized HTT1800 for ratio 2.5 can be described by the general formula $Si_{1.0}Ti_{0.3}C_{3.0}N_{1.6}H_{8.5}$ (LALE *et al*., 2017). This result is an indication that there is a content of unreacted titanium, as only 12.9 wt% of Ti is incorporated in final polymer composition, compared to the expected calculated values considering the initially amount of Ti at the synthesis reaction. As observed by Lale *et al*. (2017), the occurrence of vinyl groups lead to a steric hindrance imposed and, consequently, reduce the reactivity of this polymer with TDMAT.

In order to better elucidate the reaction mechanisms involved, sample NCHTi2.5 was selected to receive more information of the chemical structure of the polytitanosilazanes by means of NMR solid-state spectroscopy (Figure 17). Regarding the ^{29}Si NMR spectra, NCHTi2.5 polymer presents a main broad peak centred at -24 ppm that can be divided in two main groups at -21 and -29 ppm. The signal at -21 ppm is assigned to $CH_3Si(H)N_2$ and the signal at -29 ppm is due to the SiN_3C units. The signal at -29 ppm confirms that the reaction between Si-H units and NCH_3 groups from TDMAT. In addition, the polymer also contains a signal in -13 ppm which are attributed to $SiHCN_2$ group. The broad signal at -48 ppm in the ^{29}Si MAS NMR spectrum is attributed to $Si-N_4$ groups, which confirms the reaction between Si-H units and NCH_3 groups (BECHELANY *et al.*, 2014, 2017).

Figure 17 – ^{29}Si MAS NMR spectra of NCHTi2.5.
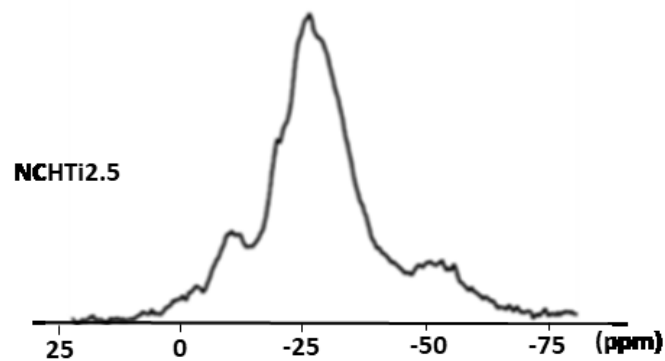
Source: Author

4.2 POLYMER TO CERAMIC CONVERSION UNDER NITROGEN

The thermal conversion of preceramic polymers into ceramics occurs in two stages through the evolution of gaseous by products involving a weight loss up on heat treatment (Figure 18).

In the case of pure silazane HTT1800, the first stage occurs between 100 and 200 °C, where the elimination of low molecular weight volatile oligomers takes place. At temperatures between 200 and 450°C, the release of NH_3 and H_2, due to the

transamination and dehydrocoupling crosslinking reactions respectively, leads to the second stage of weight loss (COLOMBO *et al.*, 2010; FLORES *et al.*, 2013). At temperature higher than 450 °C, reactions involving the cleavage of Si-H, Si-CH$_3$ and Si-CH$_2$-Si bonds occur, with the escape of hydrocarbons and hydrogen and the formation of Si-N units. This stage is represented by the transformation of the precursor polymer into an amorphous SiCN ceramic (FLORES *et al.*, 2013). After 750 °C, no weight loss is detected in TGA equipment and only molecular rearrangements occur.

TGA/MS of polyorganotitanosilazanes precursor under nitrogen in Figure 18 shows a different ceramic conversion process, giving a ceramic yield of 70 wt% and 42 wt% at 1000°C for the Si-C-N-Ti ceramic with ratio of 2.5 and 1.0 respectively. TGA curves for polytitanosilazanes display similar behaviour, however, with a significant increase of the weight losses in the range of 150 to 300 °C for sample NCHTi1.0, mostly due to higher amount of unreacted TDMAT. For this reason, sample NCHTi2.5 was used for further investigations.

Figure 18 – Thermogravimetric analyses of polysilazane and polytitanosilazanes in nitrogen.
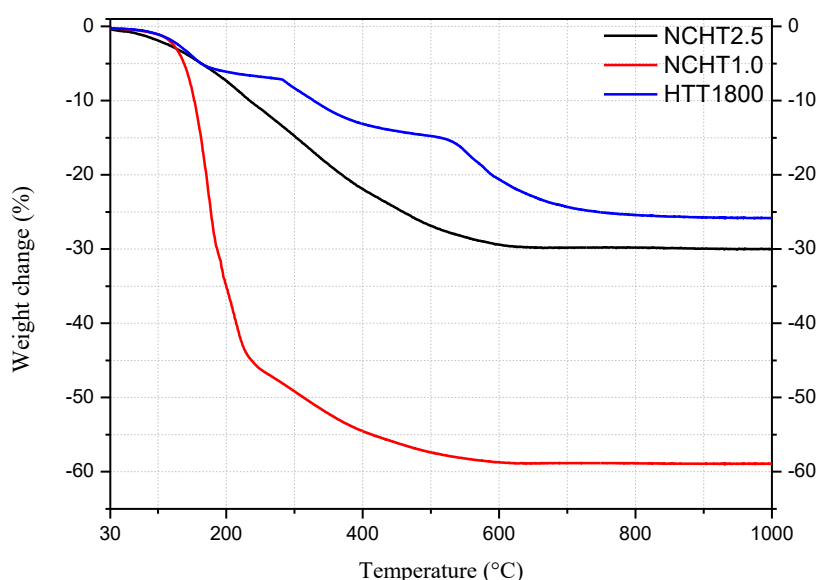
Source: Author

During ceramization process of polytitanosilazanes, especially in the temperature range from 200 to 600 °C, strong evolution of hydrogen (m/z 2) and methane (m/z 15 and 16) are detected via MS (Figure 19). The H$_2$ evolution probably

arises by dehydrocoupling reactions from the homolytic cleavage of the Si-H and N-H groups, leading to H radicals. In relation to methane releasing, the most probable reaction may arise from the degradation of the Si-CH-(CH_2) and N-CH_3 units and also between reactions of Si-H units and $N(CH_3)_2$ groups (BAHLOUL *et al*., 1993; PROUST *et al*., 2016). In the same temperature range, with an intensity relatively low, hydrocarbons and amines derivatives can be assigned for m/z 25, 26, 38, 39, 41, 42, 43, 44 and 45, indicating that transamination processes occur during pyrolysis (Figure 19) (IONESCU *et al*., 2012).

The polytitanosilazanes were pyrolyzed at different temperatures and characterized by FTIR spectroscopy (Figure 20). According to the FTIR spectra, it is possible to observe the N-H, C-H and Si-H bond stretching bands decreases in intensity with temperature increment, which indicates the occurrence of mainly dehydrocoupling and transamination reactions during pyrolysis. Bands related to the N-H, C-H and Si-H bond stretching bands can not be seen above 700 °C, which suggest that the conversion of polymer into ceramic are completed.

Figure 19 – Mass spectra of the pyrolysis of the polytitanosilazanes (ratio 2.5).
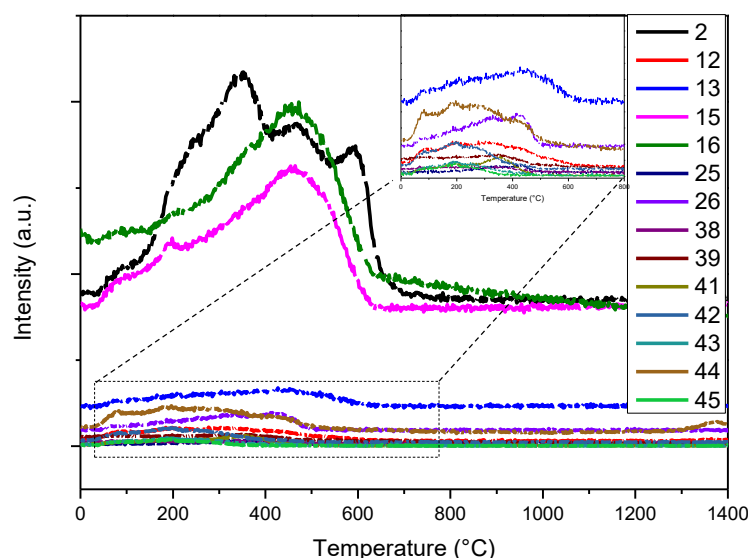
Source: Author

Figure 20 – FTIR spectra of pyrolysis intermediates from NCHTi2.5.
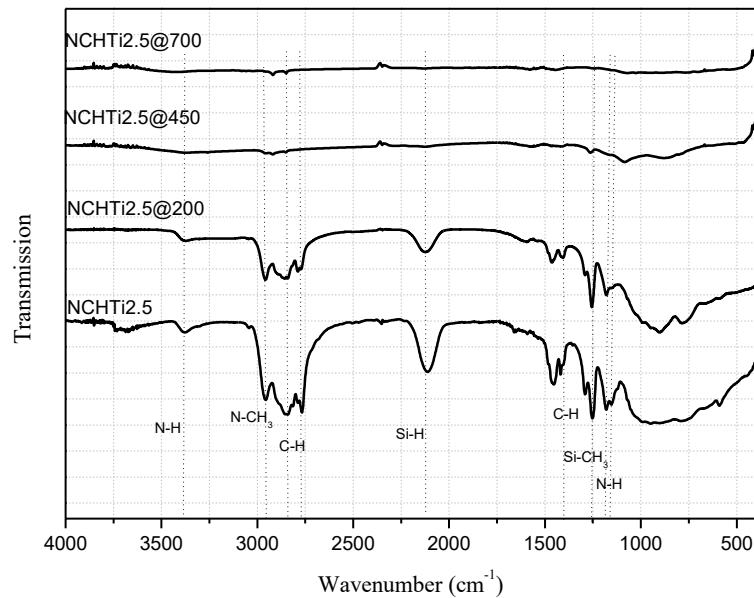
Source: Author

4.3 POLYMER TO CERAMIC CONVERSION IN AMMONIA

The thermal conversion of the preceramic polymers was also tested by a TGA in ammonia atmosphere. As it is possible to note, the TGA curve of HTT180 exhibits a similar shape as in nitrogen, although the overall weight loss is greater when NH_3 is used. The first stage (between 150 and 400 °C) corresponds to the elimination of low molecular weight volatile oligomers and formation of crosslinks. The second step occur between 400 and 700 °C and it is characterized for amination and carbon removal with hydrocarbons release. At temperature below 500 °C, reactions involving the cleavage of Si-H, Si-CH$_3$ and Si-CH$_2$-Si bonds occur, leading to the escape of hydrocarbons and hydrogen and to the formation of Si-N units (Eq. 9, 10, 11 and 12). Finally, above 700 °C, the third period is represented by a large escape of hydrogen cyanide, formed by reaction of free carbon with ammonia (Eq. 13) (Figure 21) (YIVE *et al.*, 1992)

$$Si - R + (NH_3) \rightarrow SiNH_2 + RH \tag{9}$$

$$Si - R \rightarrow \; \equiv Si\bullet + R\bullet \qquad\qquad (10)$$

$$R\bullet + NH_3 \rightarrow RH + \bullet NH_2 \qquad\qquad (11)$$

$$Si\bullet + \bullet NH_2 \rightarrow \; \equiv SiNH_2 \; (R = H, CH_3, CH_2\text{-}Si) \qquad\qquad (12)$$

$$C_{free} + NH_3 \rightarrow HCN + H_2 \qquad\qquad (13)$$
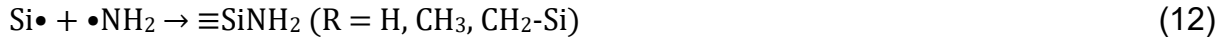
In relation to the thermodegradation there is a relative high weight loss comparing with TGA under nitrogen, which is probably due to the carbon content of pyrolysis products, which is further reduced in ammonia treatment (SONG; ZHAO; LU, 1994). The weight loss of the polytitanosilazanes is higher than pure HTT1800.

Figure 21 – Thermogravimetric analyses of polysilazane and polytitanosilazane in ammonia.
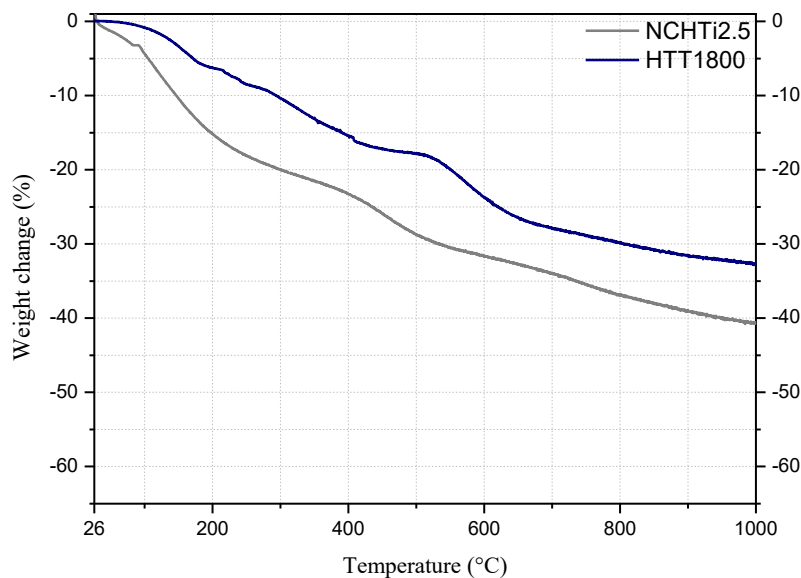
Source: Author

Polymer-ceramic conversion process of the synthesized polytitanosilazanes was investigated using FTIR spectroscopy. The FTIR spectra of the powders pyrolyzed in ammonia at different temperatures are shown in Figure 22. The crosslinking with

ammonia up to 200 °C involves the reduction in intensity of C-H band, suggesting the occurrence of transamination reactions when temperature increases (Eq. 14 and 15).

From 200 to 450 °C, the absorption band attributed to N-H bond increases in intensity probably because of the condensation of as-formed –NH$_2$ groups forming NH units (Eq. 15). Furthermore, the absorption intensities of C-H and Si-H obviously decrease at 2790 and 2100 cm^{-1} respectively, as shown in Figure 22. When temperature rises to 700 °C, the bands from N-H and Si-H groups have completely disappeared, suggesting the polymer into ceramic is almost completed.

$$\equiv Ti\text{-}N(CH_3)_2 + NH_3 \rightarrow \equiv Ti\text{-}NH_2 + N(CH_3)_2 \tag{14}$$

$$\equiv Ti\text{-}NH_2 + \equiv Ti\text{-}NH2 \rightarrow \equiv Ti\text{-}NH\text{-}Ti\equiv + NH_3 \tag{15}$$

After the heat treatment in ammonia the band at 2955 and 2912 cm^{-1} are attributed to C-H asymmetric and symmetric stretching disappears. This result indicates that most of the carbon groups are removed during pyrolysis with ammonia.

Figure 22 – FTIR spectra of Pyrolysis intermediates from NCHTi2.5 in ammonia.
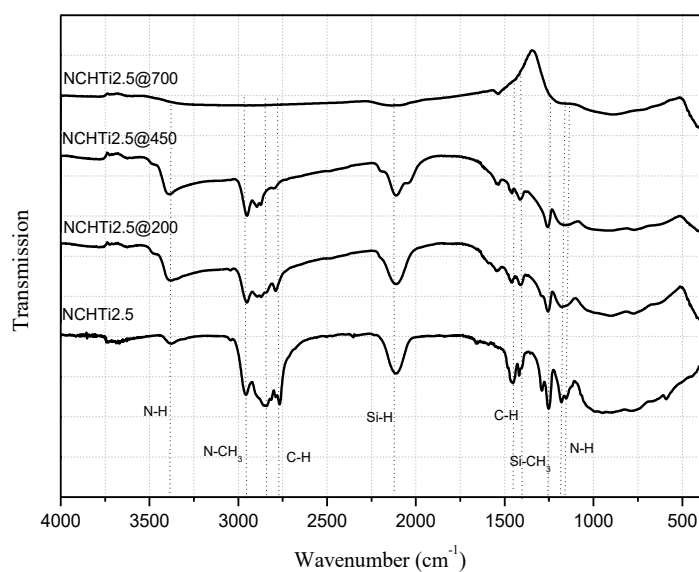
Source: Author

In order to illustrate the mechanisms involved in ammonia heat-treatment, polytitanosilazanes pyrolyzed at temperature of 450 and 1000 °C are characterized by ^{29}Si solid-state NMR spectroscopy. Figure 23 shows that the SN$_3$C unit (-29 ppm) is the major building block for ceramics at 400 °C, which confirms the reaction between Si-H units and NCH$_3$ groups from TDMAT (Eq. 2) (BECHELANY *et al*., 2017). At 450 °C, the material also contains a signal in -7 ppm which is attributed to SiN$_2$C$_2$ group.

On increasing the temperature to 1000 °C, it can be detected a shift of the signal, due to the formation Si-N$_4$, which is reflected on ^{29}Si solid-state NMR spectra of the NCHTi2.5 (BURNS; CHANDRA, 1989). In conclusion, the ^{29}Si solid-state NMR signals confirms the modification of the polytitanosilazanes after exposure to ammonia, resulting in the formation of a silicon nitride ceramic.

Figure 23 – ^{29}Si solid-state NMR spectra of the pyrolysis intermediates from NCHTi2.5.

NCHTi2.5 450°C

NCHTi2.5 1000°C

| 50 | 25 | 0 | -25 | -50 | -75 | -100 | -125 | (ppm) |
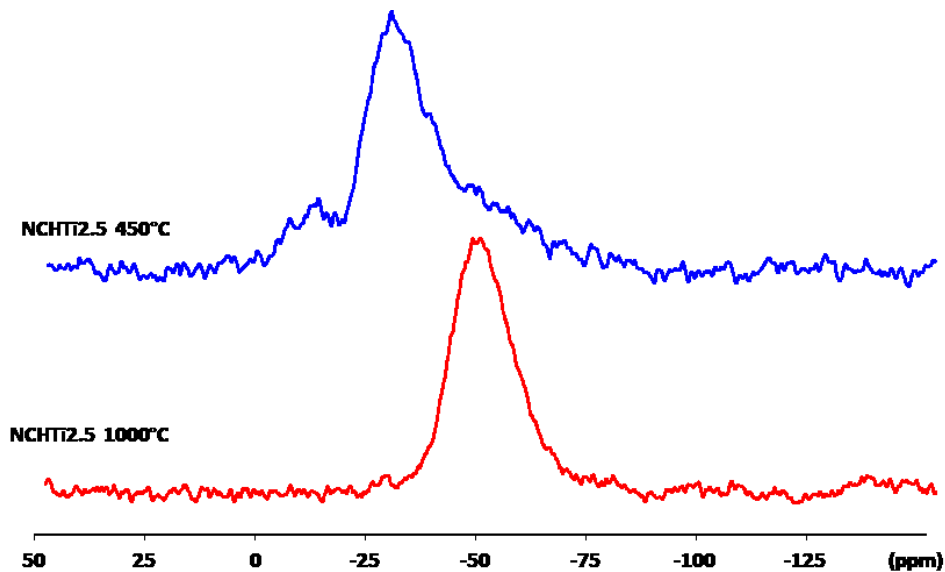
Source: Author

4.4 CHARACTERIZATION OF NITROGEN-TREATED CERAMICS POWDERS FROM 1000 TO 1500°C

Raman spectroscopy investigations evidently display the presence of free carbon of ceramic sample at 1000 °C in the bands at approximately 1305 and 1600 cm^{-1}, characteristic of sp^2 carbon. It can be observed a peak of crystalline TiC$_x$N$_{1-y}$,

normally seen at 209 and 300 cm^{-1} as a representative of the transverse acoustic (TA) and longitudinal acoustic (LA) modes are observed (Figure 24) (BARSHILIA; RAJAM, 2004).
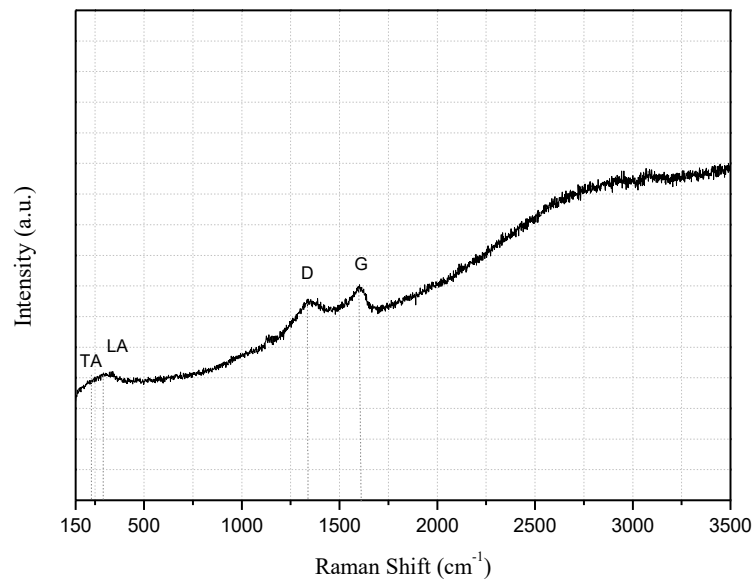
Figure 24 – Raman spectroscopy measurements of NCHTi2.5 pyrolyzed under nitrogen at 1000 °C.

Source: Author

The diffraction patterns of Si-C-N-Ti ceramics sintered at different temperatures are presented in Figure 25. The analysis shows that the samples are amorphous up to 1200 ° C. At 1400 °C, NCHTi2.5 sample has broad and weak peaks in the XRD pattern. When the pyrolysis temperature is increased at 1500 °C, The XRD pattern of NCHTi2.5 shows sharper and more intense TiC$_x$N$_{1-y}$ peaks. These peaks correspond to the face-centered cubic (fcc) TiC$_x$N$_{1-y}$ phase which appear at 36.6 °(111), 42.5 ° (200), 61.7 ° (220), 73.9 ° (311) and 77.4 ° (222) in the XRD pattern.

Analysing the XRD pattern, it is observed that no Si$_3$N$_4$ or SiC crystalline phases are detected up to 1500 °C. Probably, the presence of dispersed TiC$_x$N$_{1-y}$ nanocrystalline phases can stabilize the amorphous Si-C-N ceramics and delay or avoid the crystallization of SiCN ceramics. This indicates the Ti content has a major influence on crystallization of SiCN ceramics under nitrogen. This finding coincides

with Lale *et al.* (2017) who studied the behavior of TiN/Si$_3$N$_4$ nanocomposites pyrolyzed under ammonia.

Based on XRD analysis, we demonstrate that the samples are nanocomposites of a TiC$_x$N$_{1-y}$ nanophase embedded in an amorphous SiCN matrix. The average TiC$_x$N$_{1-y}$ nanocrystal size have been estimated using the dominant peak TiC$_x$N$_{1-y}$ (111) in the XRD data and calculated by the Scherrer equation. The calculated average crystallite size is 2.66 nm and 3.42 nm at 1400 and 1500 °C, respectively. The sizes are quite similar and small, which suggests a very low degree of crystallization.

Figure 25 – XRD measurement of the NCHTi2.5 pyrolyzed in nitrogen at different temperatures.
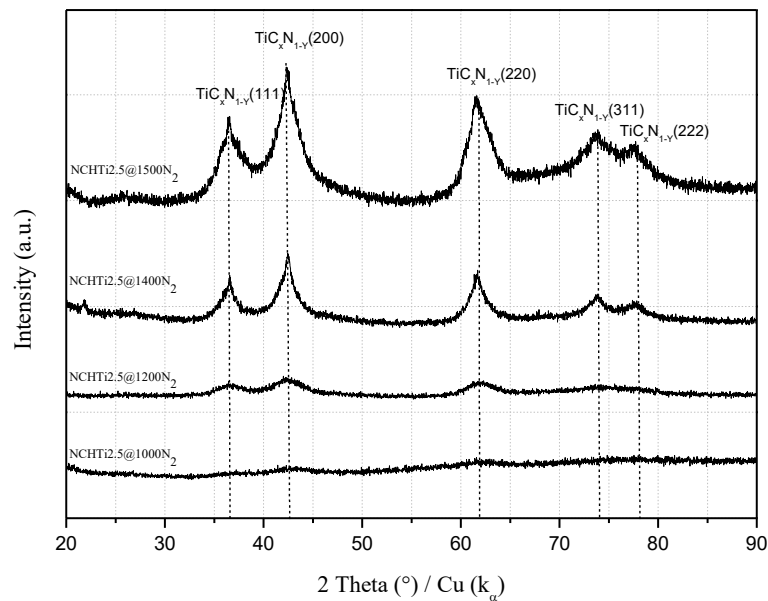
Source: Author

The diffraction patterns are further supported by TEM to provide complementary information about the morphological and crystallographic formation. Samples pyrolyzed at 1400°C and 1500°C with ratio 2.5 were selected for TEM analysis. TEM investigation of the samples pyrolyzed at 1400 °C shows a well distributed of TiC$_x$N$_{1-y}$ nanocrystals in an amorphous SiCN ceramic matrix (Figure 26), which is in agreement with XRD results (Figure 25).

Figure 26 – TEM micrographs (left) and SAED pattern (right) of sample NCHTi2.5@1400N2.
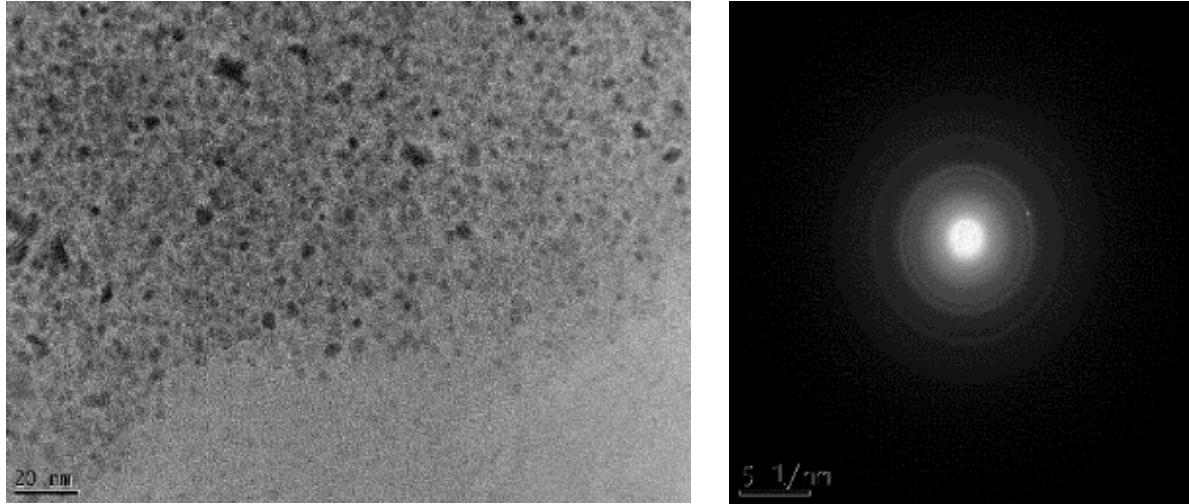
Source: Author

The SAED shows continuous rings with some weak diffraction spots, which are described to the diffractions of fcc TiC_xN_{1-y} (Figure 26). Figure 27 clearly exemplifies the homogeneous distribution of TiC_xN_{1-y} nanocrystals. This can be compared to average crystallite size estimated from XRD. The fcc structure of TiC_xN_{1-y} nanocrystals has a fringe spacing of 0.22 nm, corresponding to the d-spacing to the (200) plane of TiC_xN_{1-y}. The average crystal size is 4.3 nm with a standard deviation of 1.4 nm, indicating that the crystallite size is relatively similar to the particle size calculated by Scherrer formula from XRD data.

Figure 27 – TEM micrographs showing in detail the formation of TiC_xN_{1-y} in an amorphous SiCN ceramic of sample NCHTi2.5@1400N2.
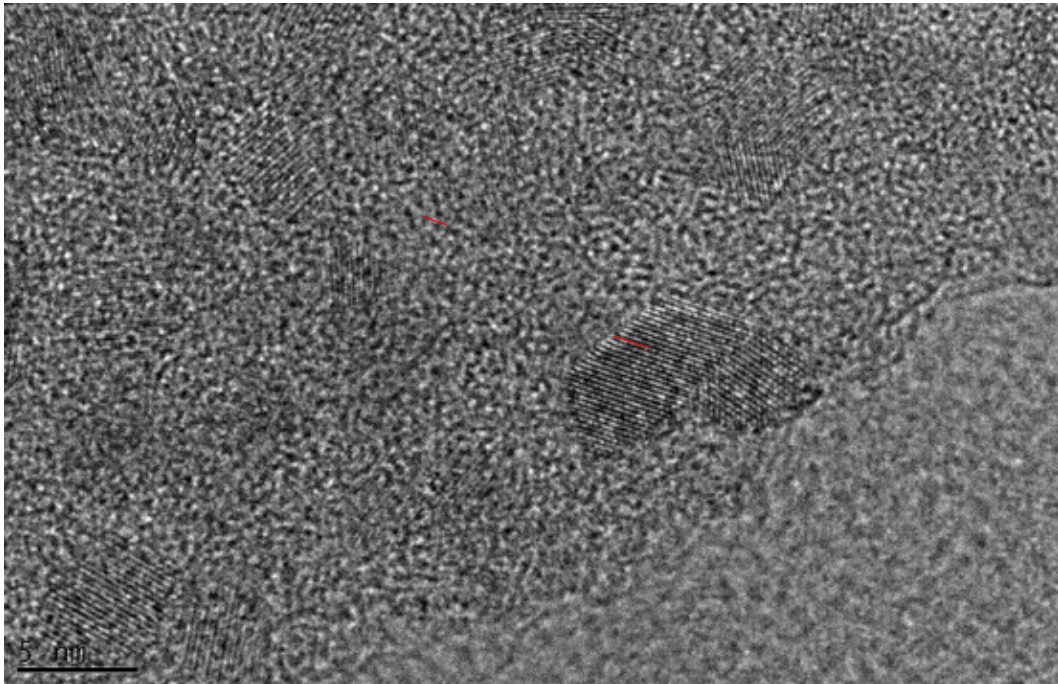
Source: Author

TEM image and SAED taken from the sample NCHTi2.5 annealed at 1500°C are shown in Figure 28. The image reveals the formation of nanocrystalline TiC_xN_{1-y}, which are dispersed in an amorphous SiCN ceramic matrix.

Comparing the average crystallite size estimated from XRD is compared with TEM micrograph displayed in Figure 28, NCHTi2.5 sample show TiC_xN_{1-y} nanocrystals with sizes distribution varying from 4.5 to 34.4 nm inserted in an amorphous matrix. This result indicates that the crystallite size is relatively higher to the particle size calculated by Scherrer formula from XRD data.

The SAED exhibits continuous ring pattern with distinct spots (Figure 28). The observed ring pattern could be attributed to the diffractions the fcc TiC_xN_{1-y} nature of the matrix. The spots present in the rings highlight the presence of TiC_xN_{1-y} nanocrystals.

TiC_xN_{1-y} nanocrysalline from Figure 29 has a d-spacing of 0.25 nm (red lines), which is in agreement with the (111) crystallographic planes of TiC_xN_{1-y}. TiC_xN_{1-y} nanocrystals are aggregates with a degree of crystallinity higher for samples annealed

at 1500 °C than 1400 °C. This is a strong evidence that the temperature of pyrolysis promotes the crystal growth of TiC_xN_{1-y} nanocrystals. However, even at the highest temperatures, none of the specimens were fully crystallized. Based on TEM and SAED patterns investigations, no crystallites related to silicon carbide or silicon nitride are detected at 1500 and 1400 °C, which is in agreement with XRD patterns.

Figure 28 – TEM micrographs (left) and SAED pattern (right) of sample NCHTi2.5@1500N2.
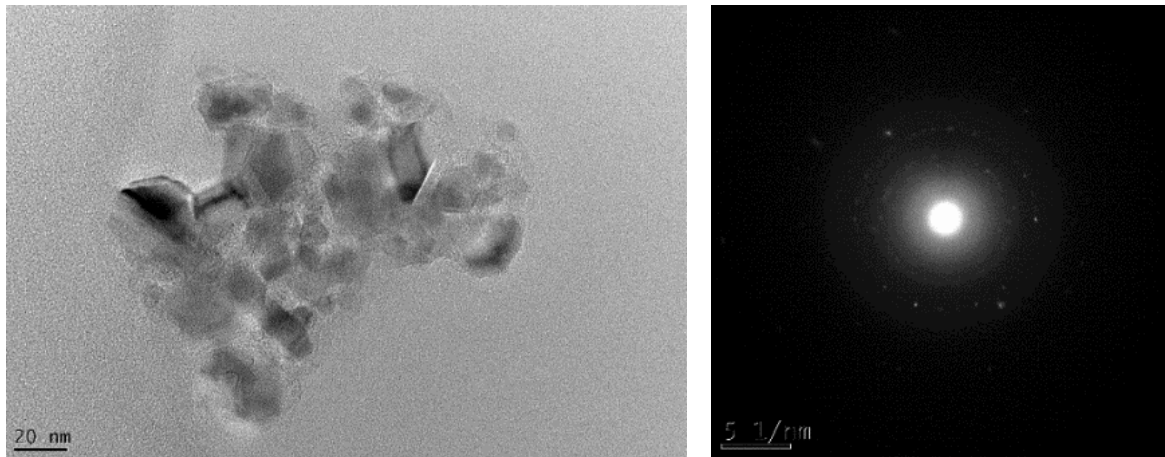
Source: Author

Figure 29 – TEM micrographs showing in detail the TiC_xN_{1-y} nanocrystal of sample NCHTi2.5@1500N2.
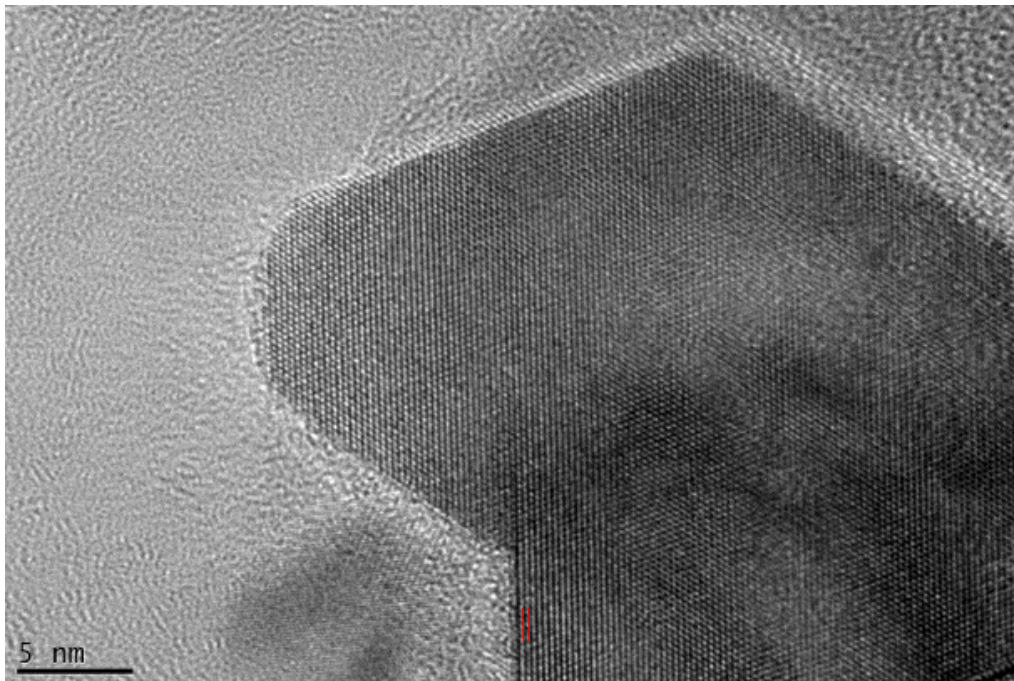
Source: Author

4.5 CHARACTERIZATION OF AMMONIA-TREATED CERAMICS POWDERS FROM 1000 TO 1500 °C

The Raman spectra of the powders pyrolyzed at 1000 °C in ammonia are shown in Figure 30. The scattering peak at 275 cm^{-1} is assigned to first-order transverse acoustic (TA) and to the longitudinal acoustic (LA) of TiN. The peak at 560 cm^{-1} arises from the transverse optic/longitudinal optic (TO/LO) mode.

As reported by Cheng *et al*. (2002), TA and LA modes are determined by vibration of Ti ions whereas TO mode is related to vibrations of N ions. The peak at 440 cm^{-1} arises from the second-order acoustic (2A) mode. No significant peaks bands of sp^2 carbon are observed at approximately 1305 and 1600 cm^{-1}. These results confirm the growth of the TiN nanophase and suggests that most of the free-carbon are removed under pyrolysis in ammonia.

Figure 30 – Raman spectroscopy measurements of NCHTi2.5 pyrolyzed under ammonia at 1000 °C.
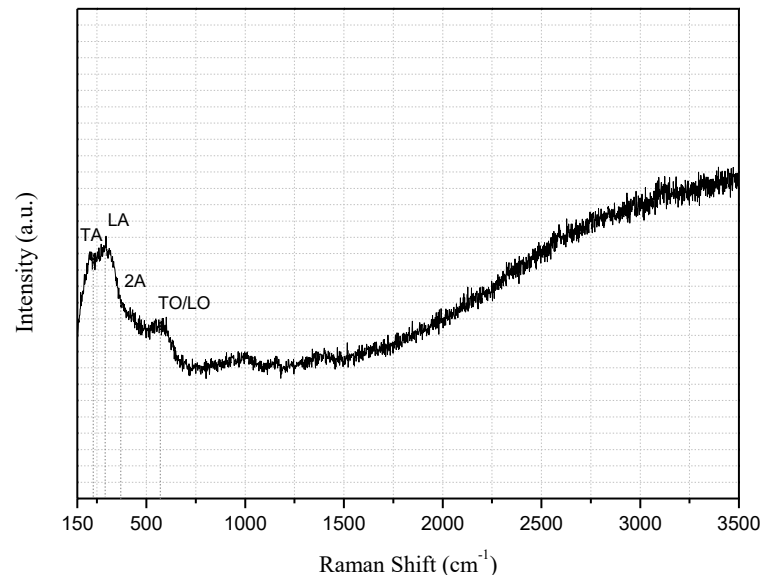
Source: Author

Pyrolysis temperature under ammonia has a significant impact on the structure evolution on ceramics especially during its phase separation and carbothermal reduction process. The structure of pyrolytic products is completely amorphous up to 1200 °C as shown in Figure 31.

Powder XRD analysis confirms that the ammonia-treated polytitanosilazanes derived ceramics is structurally amorphous until 1200 °C. The crystallization of polytitanosilazanes powders occurs between 1400 °C and 1500 °C. At 1500°C, it is noted peaks for TiN corresponding to the nucleation of the fcc TiN phase based on file 00-038-1420, which appear at 36.6°(111), 42.5° (200), 61.7° (220), 73.9° (311) and 77.4° (222) in the XRD pattern.

The formation of small Si_3N_4 crystalline phases are detected when the temperature rises to 1500 °C. The TiN crystallite growth from 1400 to 1500 °C. An estimate of the crystallite size was obtained from TiN (111) peak using the Scherrer formula. The calculated average crystallite size is 1.93 nm and 30.24 nm at 1400 and 1500 °C, respectively.

Figure 31 – XRD measurement of the powders pyrolyzed in ammonia at different temperatures.
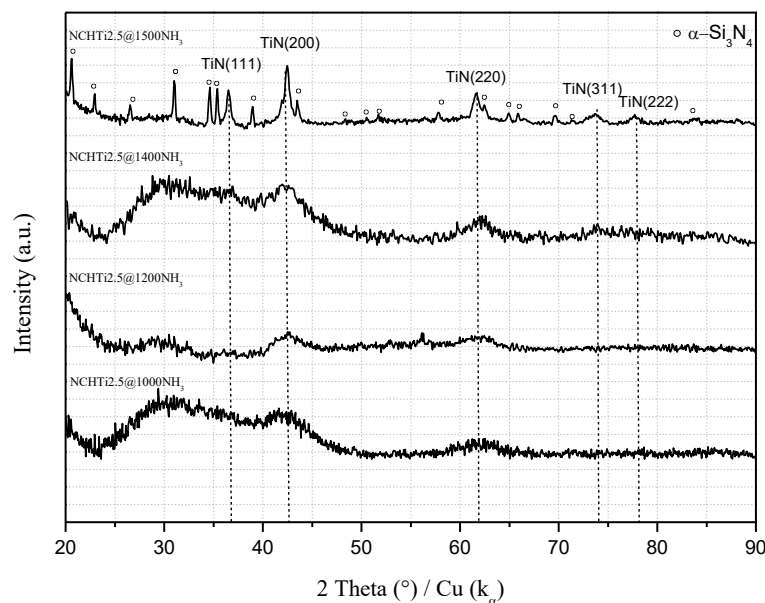
Source: Author

The microstructure of the powders pyrolyzed in ammonia at 1400 °C and 1500 °C is examined by TEM. These images reveal the presence of TiN nanocrystals dispersed in a silicon nitride matrix.

As shown in Figure 32, the size of the TiN nanocrystal is around 10 nm, with an interplanar spacing close to 0.22 nm (red arrows), which can be attributed to (200) lattice plane of TiN in agreement with the X-ray data. Furthermore, there is also the presence of crystallites embedded in amorphous matrix, which are proved to be α-Si_3N_4 nanocrystalline (blue arrows). The well-crystallized α-Si_3N_4 are clearly observed in Figure 33.

Figure 32 – TEM micrographs of sample NCHTi2.5@1400NH_3 showing the presence of TiN.
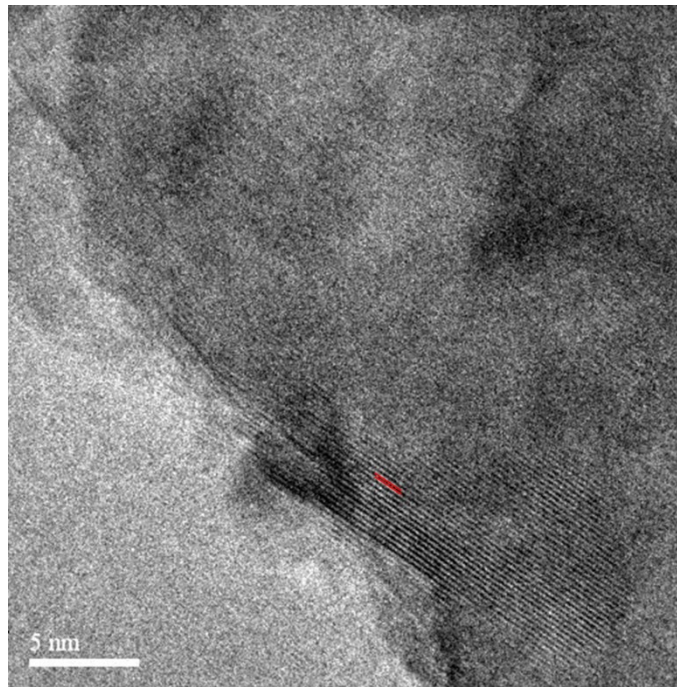
Source: Author

Figure 33 – TEM micrographs of sample NCHTi2.5@1400NH$_3$ showing the presence of α-Si$_3$N$_4$ nanocrystalline.

Source: Author

Increasing pyrolysis temperature promotes the crystal growth of TiN nanocrystals. The image from Figure 34 reveals nanocrystals with relatively larger sizes, which were dispersed on Si$_3$N$_4$ matrix. High-resolution TEM of samples pyrolyzed at 1500 °C shows a clear visualization of TiN structure embedded in a Si$_3$N$_4$ matrix (Figure 35). The distance between these planes is 0.22 nm that is the same as the (200) lattice planes in TiN crystalline. HRTEM also confirms the presence of Si$_3$N$_4$ nanocrystallites with a measured interplanar distance of approximately 0.37 nm. This result agrees with XRD characterization.

Figure 34 – TEM micrographs of sample NCHTi2.5@1500NH$_3$.
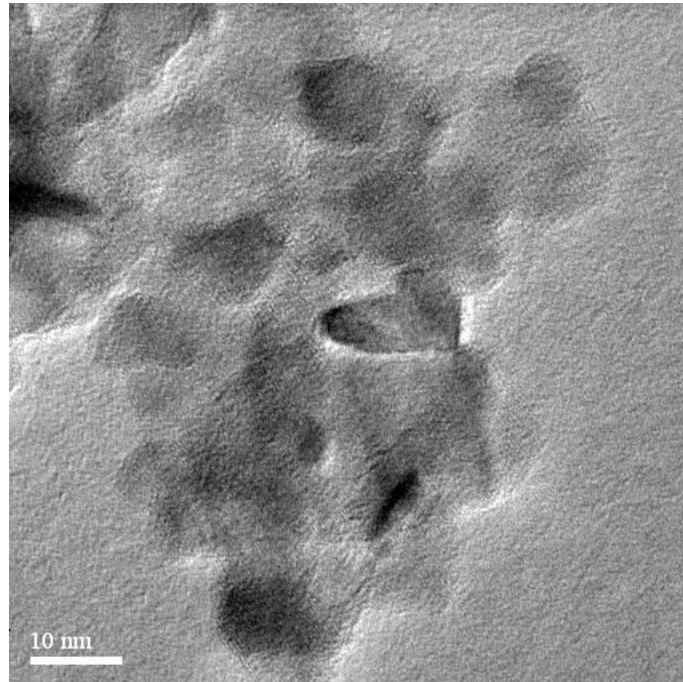
Source: Author

Figure 35 – TEM micrograph of sample NCHTi2.5@1500NH$_3$ showing in detail the presence of TiN.
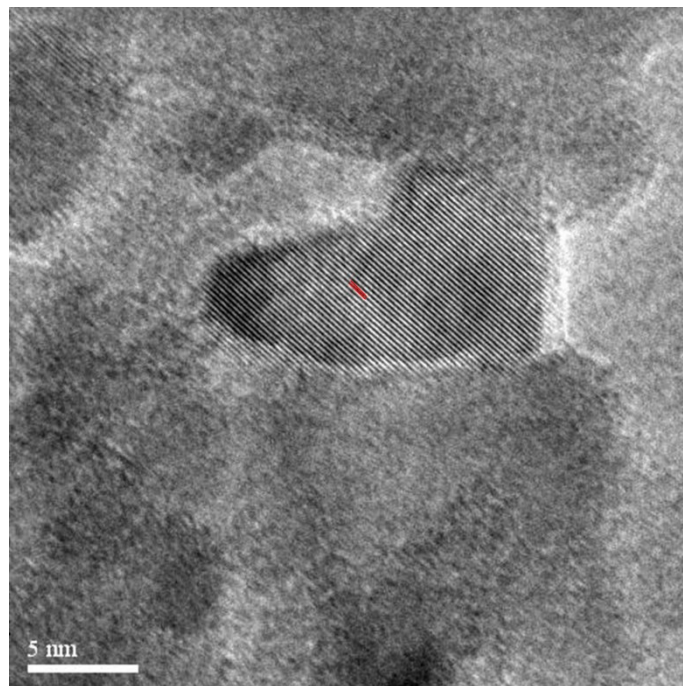
Source: Author

4.6 DESIGN OF MICRO-/MESOPOROUS SAMPLES USING ACTIVATED CARBON MONOLITHS

Preparation of monolith with tailored mesoporosity was done with impregnation of the ACM porous structure with a preceramic polytitanosilazane solution by nanocasting method. Based on previous studies that evaluated the effect of the mass ratio, a mass polymer-to-template ratio of 1.4 is used because it represents the minimal ratio to avoid the collapse of the structure of monoliths during the pyrolysis (LALE *et al*., 2017).

Two thermal strategies are employed for the design of micro/mesoporous components. The first strategy involves the pyrolysis under nitrogen at 1000 °C and the conversion of preceramic polymer to ceramic. Through pyrolysis in nitrogen, HTT1800 leads to a composite material of Si-C-N matrix and the carbonaceous template isn't removed.

The second strategy are adapted as reported by Lale and others (2017). To avoid the ACM complete decomposition in the presence of ammonia, the system is first heated at 400 °C under nitrogen to ensure sufficient conversion of the preceramic polymer to a crosslinked state to provide structural stability. After this step, the pyrolysis gas is changed to ammonia and the sample is heat-treated up to 1000 °C. Via high temperature pyrolysis in ammonia, HTT1800 leads to materials composed mainly of Si_3N_4 and the ACM template is removed. Both heat-treatments leads to TiN nanocrystals in a ceramic matrix. Subsequent annealing up at 1400°C under nitrogen leads to the formation of nanocomposites in which TiN nanocrystals are distributed in a ceramic matrix (Si_3N_4 in ammonia or SiCN in nitrogen).

The N_2 adsorption–desorption isotherms of synthesized materials are shown in Figure 36 and 37. All samples present a combination of type II and IV sorption, according to the IUPAC classification. These characteristics indicate that the samples contain a major proportion of micropores at lower relative pressures, which are related with type II curve, and also mesoporosity at higher relatives pressures with 3-D cage-like pores and interconnected pores, which are associated with type IV curve (SING *et al*., 1985).

Figure 36 – N$_2$ Adsorption/Desorption Isotherms of mNCHTi2.5 pyrolyzed under nitrogen at (a) 1000 °C and (b) 1400 °C.

(a)

(b)
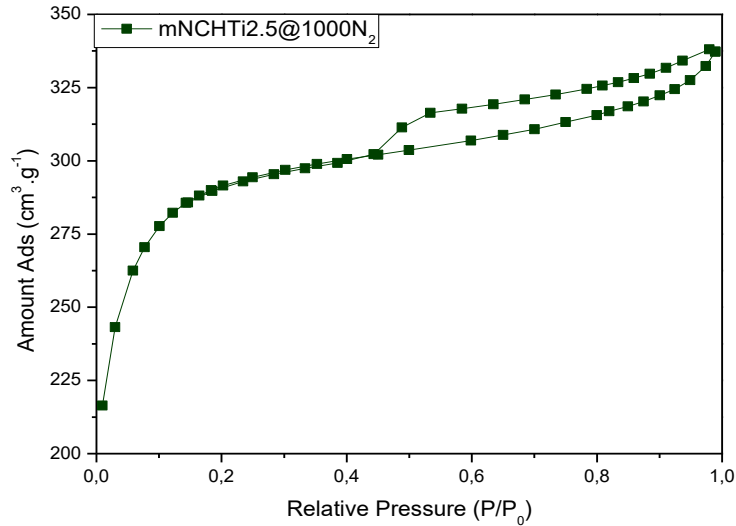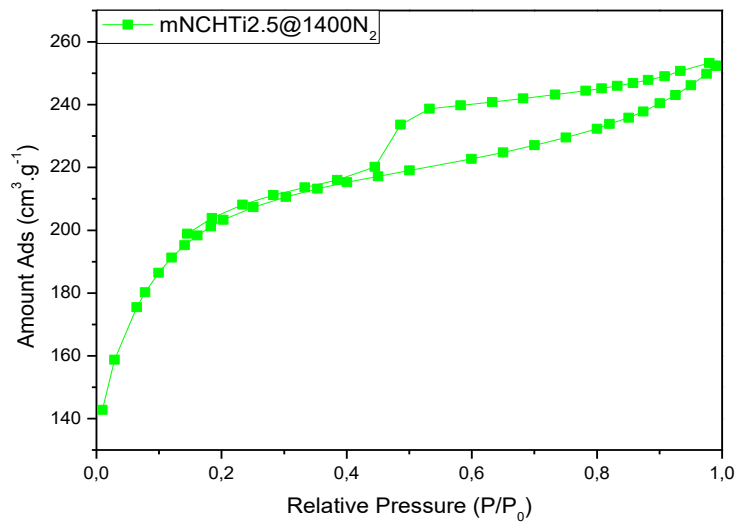
Source: Author

The curves are asymmetrical and exhibit a hysteresis loop, showing that a steeper capillary condensation step occurred at a relative pressure P/P0 of 0.40 to 1.0, indicating the presence of mesopores. The physisorption hysteresis of the samples are

classified as type H2, which can be attributed to the regular pore structures with 3D-cage-like pores based on ACM structure (SING; WILLIAMS, 2004).

Figure 37 – N$_2$ Adsorption/Desorption Isotherms of mNCHTi2.5 pyrolyzed under ammonia at (a) 1000 °C and (b) 1400 °C.

(a)

(b)
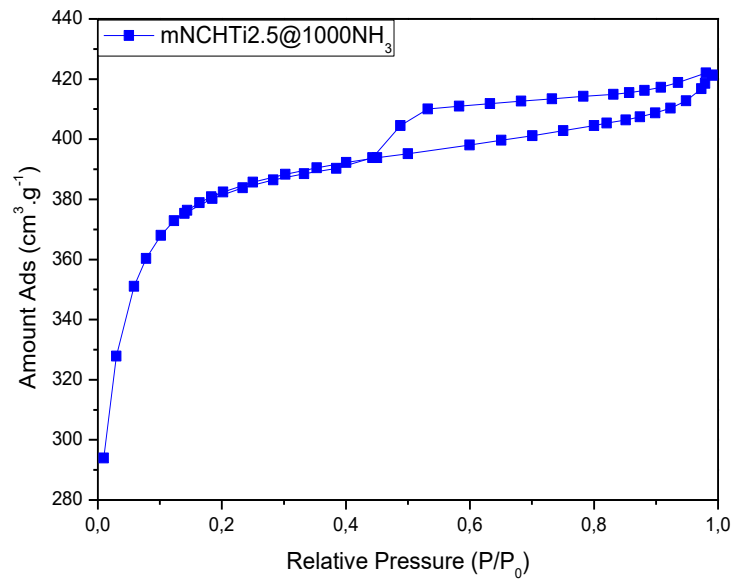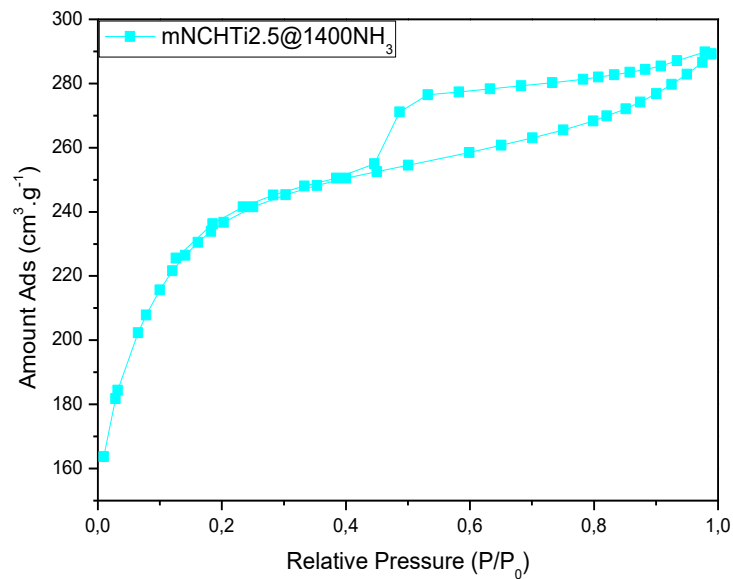
Source: Author

The BET results show the presence of interconnected micro- and mesoporosities that forms a robust material with high values of SSA for such compounds. The pore-size calculated from the desorption branch of the N_2 isotherm by BJH method are quite similar in all monoliths and exhibit uniform mesopore dimensions ranging around 3.09 and 3.49 nm (Table 3) (Figure 38). The highest value of SSA, 1244 m^2g^{-1}, was obtained for a sample with Si:Ti ratio of 2.5 and pyrolyzed at 1000 °C under NH_3.

For both ratios, the samples pyrolyzed under nitrogen show similar results in relation to pore size, surface area and micropore volume. On the other hand, it can be observed that ammonia treatment of mNCHTi2.5 samples causes an increase in BET surface area compared to the samples threated in nitrogen (Table 3). The increase in SSA is possibly due to higher carbonization temperature when exposed in ammonia and also the introduction of basic nitrogen groups which lead to rather pores enlargement (SHAFEEYAN *et al*., 2011).

In addition, the BET measurements show that mNCHTi2.5 possess higher surface area compared with mNCHTi1.0 in ammonia. As ratio 1.0 has higher amount of Ti, a considerable decrease in the SSA could be explained due to the high degree of TiN nanoparticle loading (LIU *et al*., 2011). It is noteworthy that the decrease in surface area could also be associated to the higher weight loss detected for sample NCHTi1.0. With a higher weight loss, more zones of the template would be exposed and consequently eliminated under ammonia.

The BET surface area and the micropore volume of the samples decrease with the increase of temperature, which could be attributed to the framework shrinkage of the ACM and the decrease in the volume of the pores due to the high-temperature treatment (LALE *et al*., 2016).

Figure 38 – Pore size distribution for sample mNCHTi2.5@1400NH$_3$.
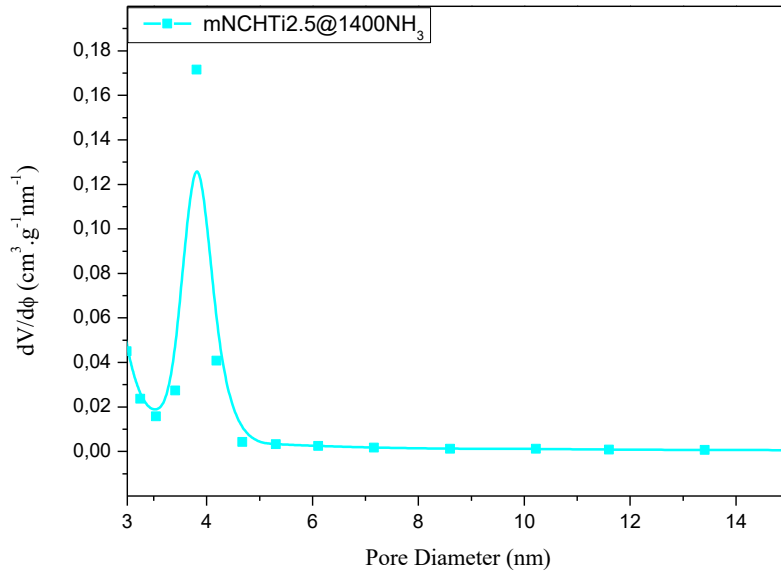
Source: Author

Table 3 – Results obtained from the N$_2$ Adsorption/Desorption Isotherms.

Sample	Pyrolysis Temperature	Gas	Surface area (m² g^{-1})	Micropore volume (cm³ g^{-1})	Pore Size (nm)
mNCHTi2.5	1400	NH$_3$	793	0.19	3.09
	1400	N$_2$	678	0.17	3.36
	1000	NH$_3$	1244	0.47	3.14
	1000	N$_2$	954	0.34	3.49
mNCHTi1.0	1400	NH$_3$	692	0.13	3.07
	1400	N$_2$	691	0.19	3.20
	1000	NH$_3$	862	0.31	3.07
	1000	N$_2$	1068	0.38	3.31

Source: Author

The high-temperature treatment involves also the crystallization of the TiC$_x$N$_{1-y}$ and TiN phase at 1400 °C under nitrogen and ammonia, respectively, as shown in the X-ray diffraction patterns of these materials. Samples pyrolyzed under nitrogen and ammonia are X-ray amorphous at 1000 °C (Figure 35 and 36).

As observed by XRD analysis, the crystallite peaks of mesoporous ceramics (Figure 39 and 40) is significantly more pronounced than powders samples (Figure 25 and 31). This difference can be attributed to the enhancement of the SSA and then increasing the interaction during pyrolysis of the material, which start to crystallize at lower temperatures (GAO *et al*., 2012).

The presence of two large bands in the samples indicate the presence of amorphous phase. The bands located at 22° and 43 °2θ correspond to the interplanar spacing (002) and the spacing between the carbon atoms in the plane (100), respectively. In addition, the monoliths also contained some graphite-like structures at 27°.

The diffraction patterns are further supported by SEM. The heat-treatment of the samples pyrolyzed under ammonia at high temperature involves the nucleation of α-Si_3N_4 phase. While crystallization of α-Si_3N_4 occurs, the formation of nanowires is observed in the monoliths (Figure 41). As reported by Lale *et al*. (2017), the formation of Si_3N_4 nanowires can also be attributed to SSA decreasing at 1400°C.

The formation nanowires is also detected for samples synthesized in nitrogen at 1400 °C (Figure 42). The SEM of sample mNCHTi2.5 shows a quantity of straight nanowires with uniform diameter, which are randomly oriented in the mesoporous structure. The average diameter is 0.74 ± 0.15 nm, and the length ranges from 10 to 100 micrometers. The presence of nanowires in the mesoporous structure could provide strongly interlocking effect between the Si-C-N-Ti ceramic matrix and the ACM as well as increasing the physical properties.

Figure 39 – XRD patterns of monoliths under ammonia at 1000°C and 1400 °C.
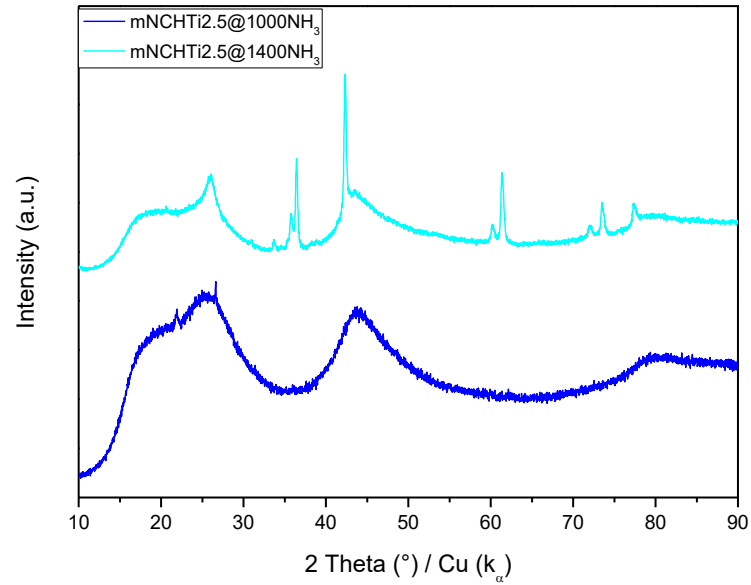
Source: Author

Figure 40 – XRD patterns of monoliths under nitrogen at 1000°C and 1400 °C.
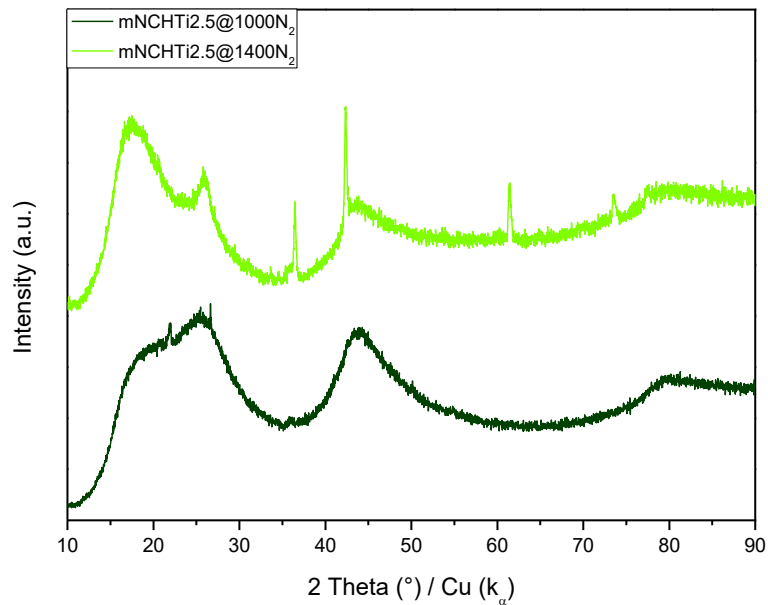
Source: Author

Figure 41 – Nanowires formation of monoliths after heat treatment at 1400 °C in ammonia.
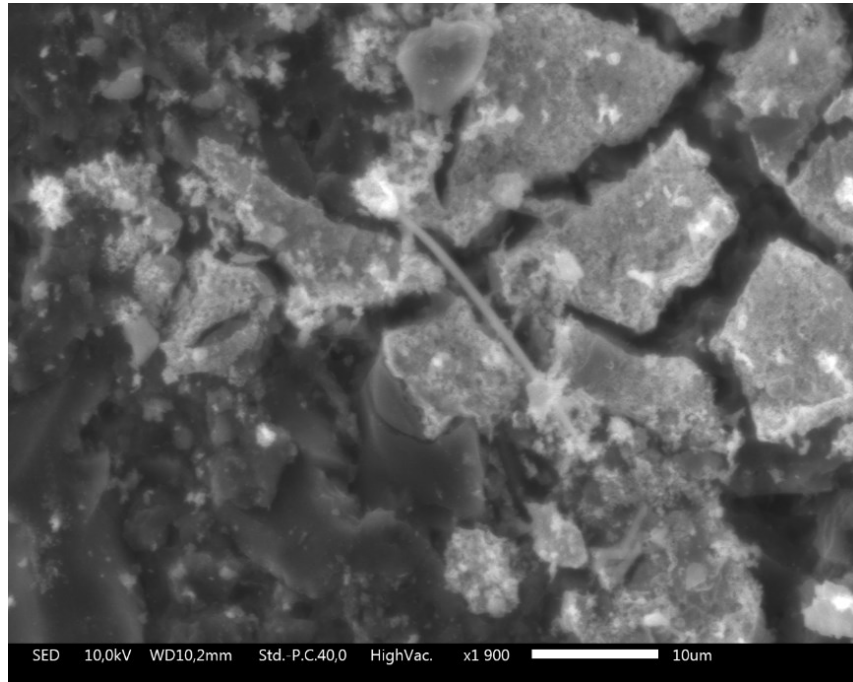
Source: Author

Figure 42 – Nanowires formation of monoliths after heat treatment at 1400 °C in nitrogen.
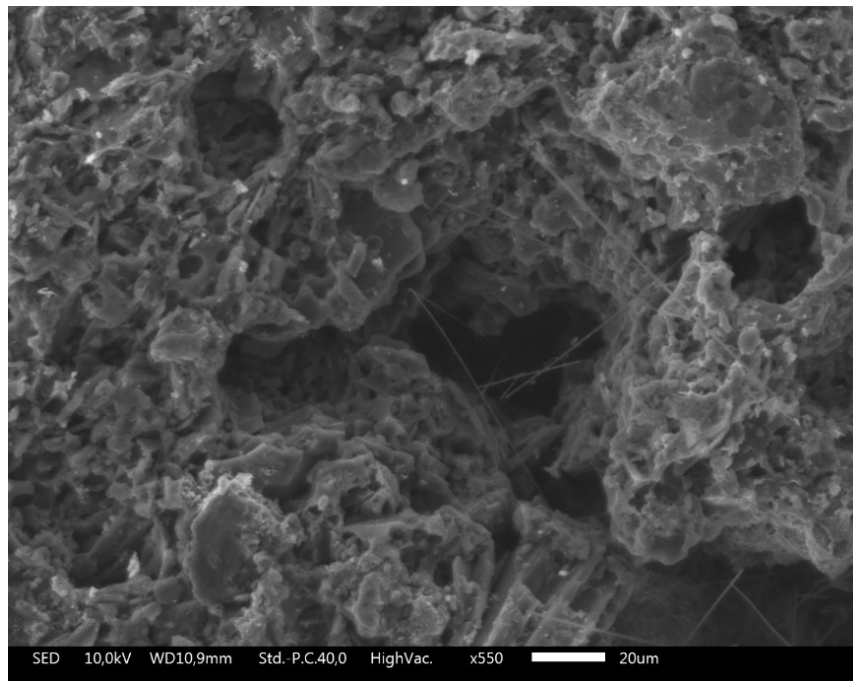
Source: Author

In order to obtain more information about the microstructure in Figure 41 and 42, elemental analysis was made by Energy Dispersive Spectroscopy (EDS) of crushed sample mNCHTi2.5@1400 under ammonia and nitrogen (Figure 43 and 44). The EDS shows a considerable high value of Carbon in the ACM template. The nitrogen content is increased in sample pyrolyzed under ammonia, generating a nitrogen-rich ceramic due to nitridation reaction. This result proves the the effectiveness of nitrogen incorporation under ammonia gas heat-treatment.

The high concentration of carbon trapped within the samples pyrolysed under ammonia demonstrates the retention of the carbon template. This is probably due to the effect of TiN particles and the Si_3N_4 ceramics phases acting as a coat, which protect the ACM surface against ammonia. As a consequence, just the free ACM without the TiN/Si_3N_4 ceramic coat is removed under ammonia. This considerable high amount of Carbon is quite similar in the system pyrolyzed under nitrogen. Through pyrolysis in nitrogen, the presence of carbon is predictable since the template is not expected to be removed during the heat treatment (Figure 43).

Figure 43 – EDS spectrum of mNCHTi2.5@1400N2 sample.
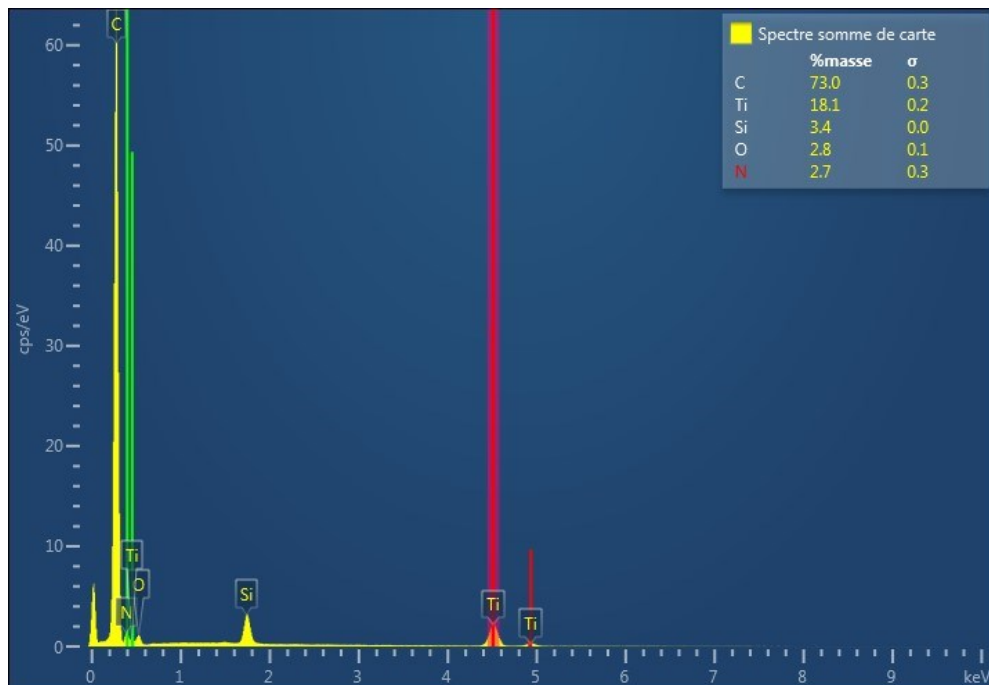
Source: Author

Figure 44 – EDS spectrum of mNCHTi2.5@1400NH3 sample.
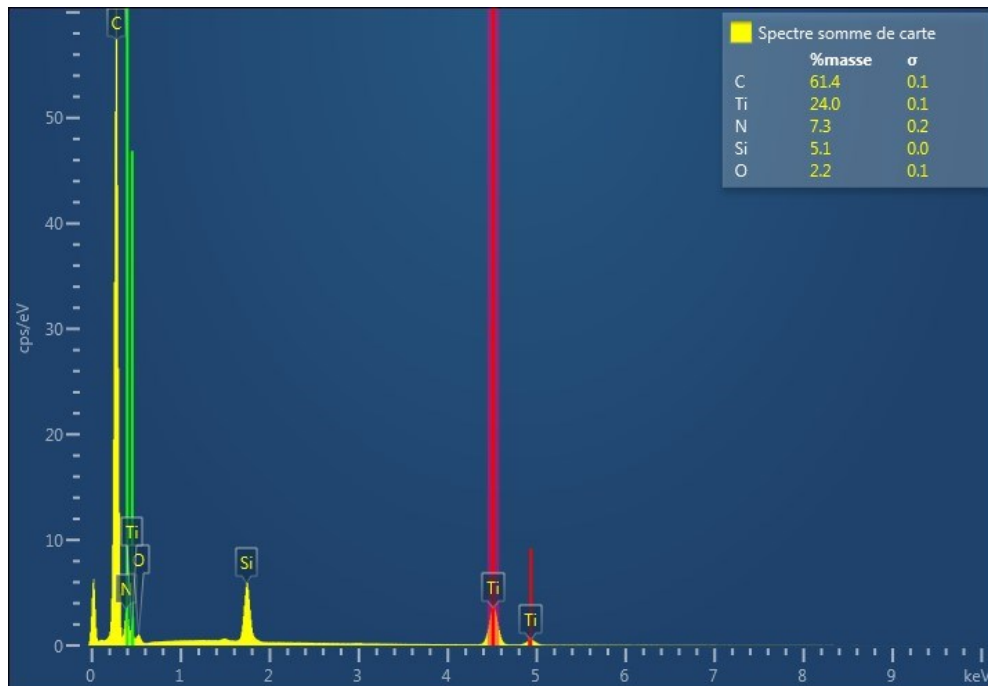
Source: Author

The occurrence of carbon phases is also confirmed by Raman spectroscopy analysis. The main bands to analyse the carbon phases are the band of disordered carbon structure, band D, at approximately 1350 cm^{-1}, and the band G at 1582 cm^{-1}, due to a relative movement of the sp^2 carbon atoms. In addition, other bands are observed in the sample spectra, such as the D' band at 1620 cm^{-1} indicating a disordered graphite network and the D'' band at 1500 cm^{-1}, which is related to the presence of amorphous carbon (CHEN *et al*., 2014; MERA *et al*., 2009).

The presence of band G and band D in Raman confirm the presence of carbon phases, even after heat treatment in ammonia. These results suggest that TiN coating is effective in protecting the template against ammonia. However, no signal is detected concerning TiN, probably due to the relatively low concentration of TiN and/or the reduced size of the TiN domains formed.

The Raman spectra were adjusted using the Gaussian and Lorentzian functions by applying Magic Plot Student version 2.7.2 software. The ID/IG ratio is obtained from the band adjustments. The La values were calculated from the Ferrari and Robertson formula and range from 1.42 to 1.59 nm (Figure 45 and 46). These

values, and consequently the ID/IG ratio, remain practically constant with the pyrolysis temperature increase (FERRARI; ROBERTSON, 2004).

Si-C-N-Ti ceramics indicate broad and strong signals as a consequence of the pronounced structural disturbance of the carbon phase. As the pyrolysis temperature increases, the D and G bands become narrower and distinct and the D' and D" bands decrease in intensity. Concomitantly, it is observed the G band and the G+D band increase the intensity, becoming more evident by increasing the pyrolysis temperature (Figure 45 and 46).

The G'' band intensity is an indicator of the degree of organization of the graphene layers and the order of stacking along the axis. Thus, as the temperature increases, occurs an increase in the organization of the carbon-free phase. However, these results indicate a remaining degree of disorder of the pyrolyzed samples up to 1400 ° C, corroborating with XRD results.

Figure 45 – Raman spectroscopy measurements of products pyrolyzed under ammonia
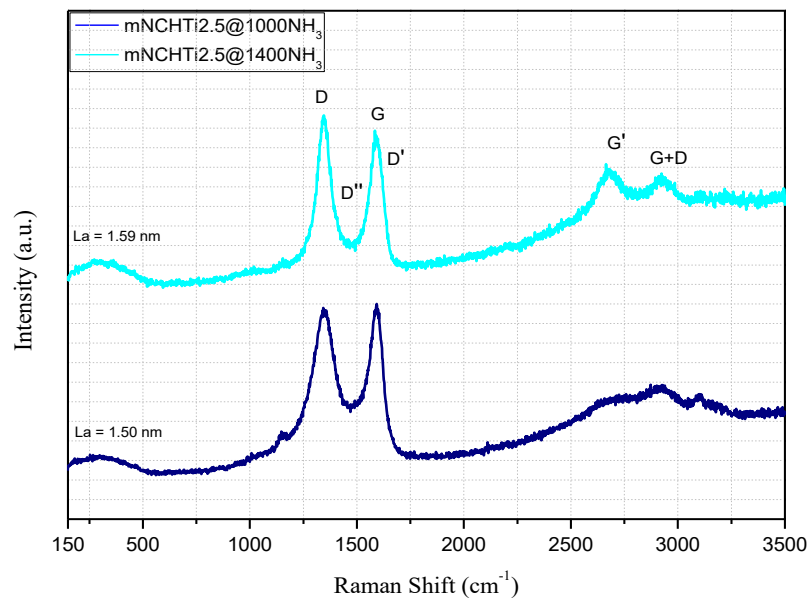
Source: Author

Figure 46 – Raman spectroscopy measurements of products pyrolyzed under nitrogen.
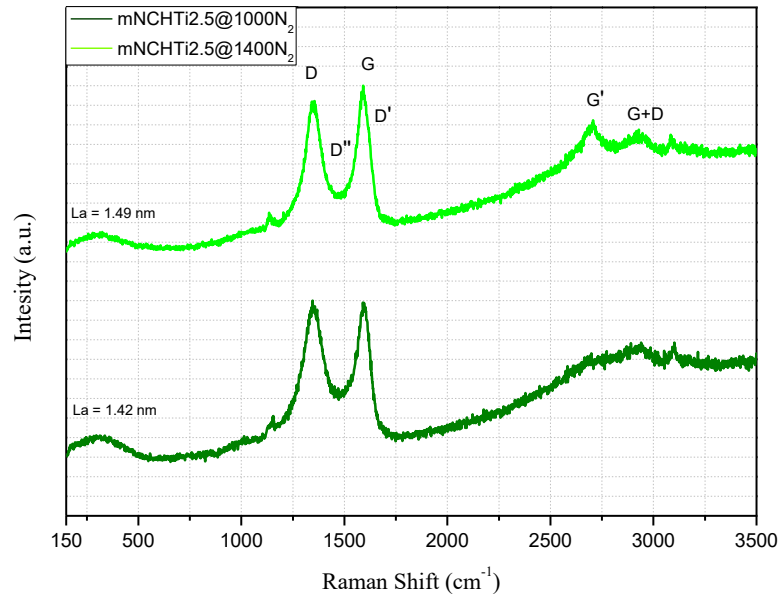
Source: Author

More information about the nanostructure on the monoliths is obtained by TEM technique. Figure 47 and 48 illustrate the TEM image for samples mNCHTi2.5@1400N$_2$ and mNCHTi2.5@1400NH$_3$, respectively.

The SAED pattern exhibits a diffuse ring characteristic for an amorphous material, which is in agreement with XRD and Raman results. However, the SAED pattern exhibits bright spots which indicate the formation of isolated nanocrystalline phases. Figure 47 and 48 show where the nanocrystallites are located in the carbon matrix. It can be observed that the nanocrystals are clearly discerned in the dark field image.

Figure 47 – TEM image (left) and dark field (right) of mNCHTi2.5@1400N$_2$ (Inset figures show the corresponding SAED pattern).
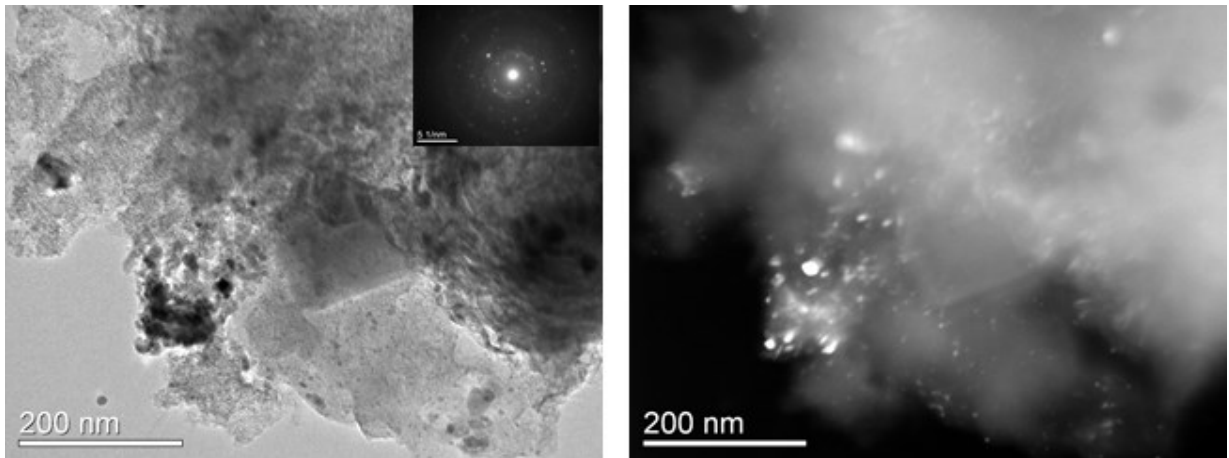
Source: Author

Figure 48 – TEM image (left) and dark field (right) of mNCHTi2.5@1400NH$_3$ (Inset figures show the corresponding SAED pattern).
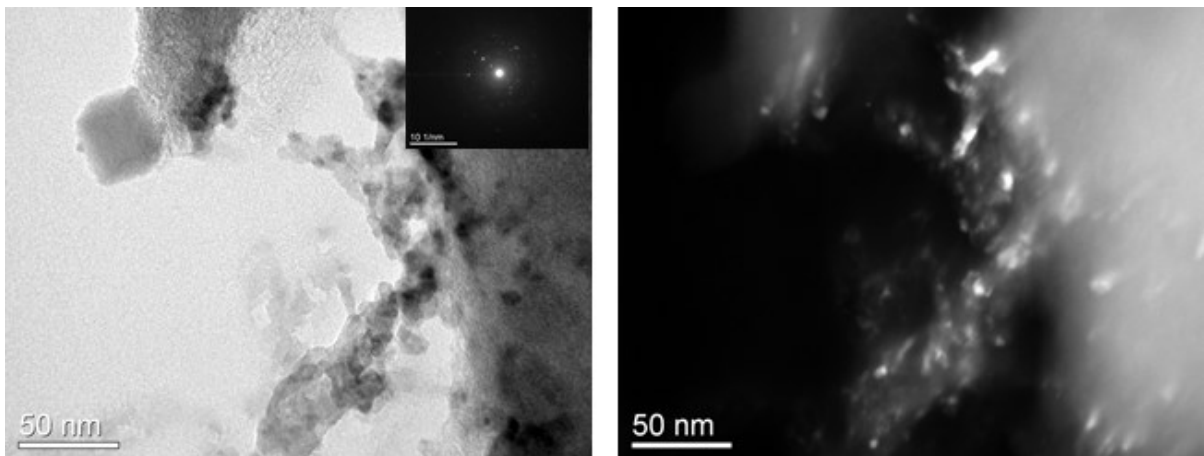
Source: Author

The monoliths is observed in more detail with the HRTEM technique. For samples pyrolyzed in nitrogen, the HRTEM image and SAED pattern demonstrate the integrity of activated carbon after pyrolysis, indicating a well distribution of the amorphous carbon phase. Figure 49 reveals that mesoporous ceramics derived activated carbon monoliths have a graphitic-like structure (green arrows). Furthermore, the mesoporous materials annealed at 1400 °C in nitrogen are composed TiC$_x$N$_{1-y}$ nanocrystallites embedded in a carbon matrix (Figure 50).

Figure 49 – HRTEM micrograph showing the formation of graphitic-like structure.
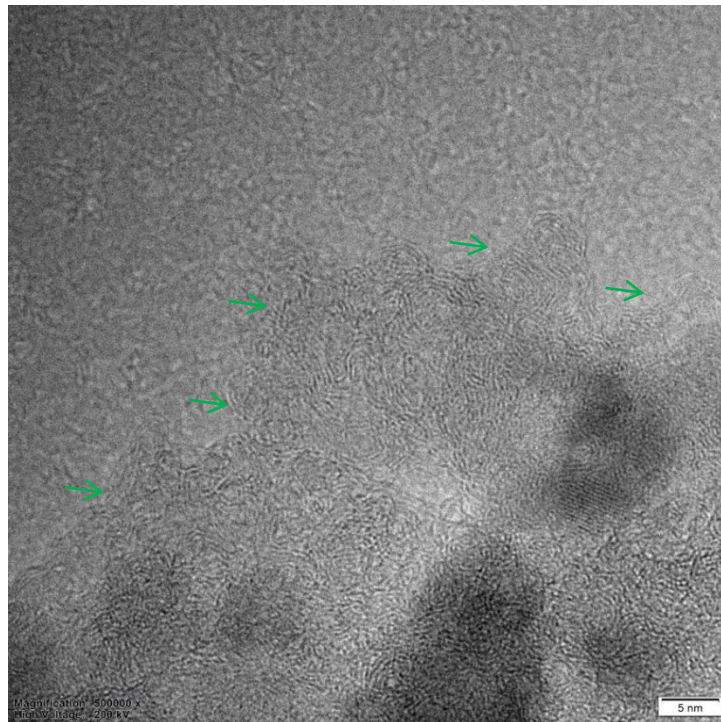
Source: Author

Figure 50 – HRTEM micrograph of mNCHTi2.5@1400N$_2$ sample.
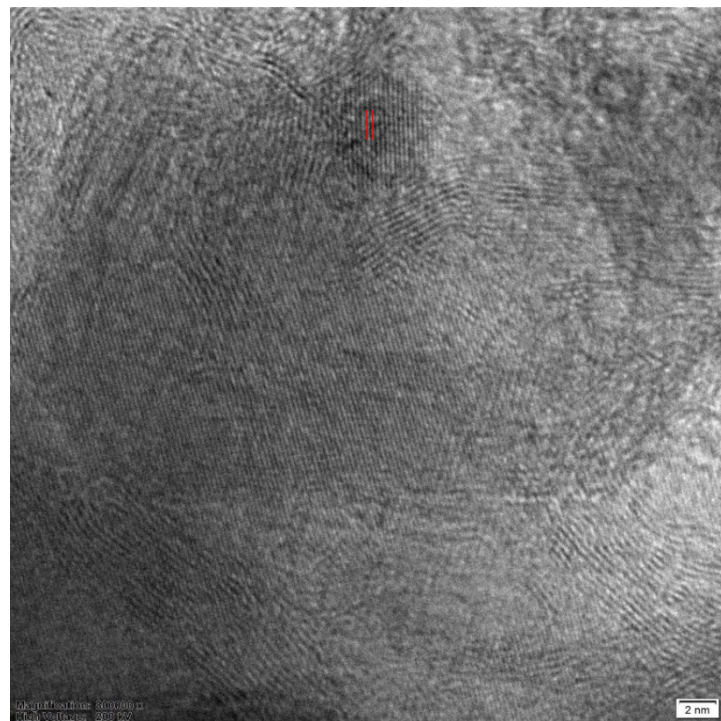
Source: Author

In the case of mNCHTi2.5@1400NH$_3$ sample, the retention of the carbon template can be observed. The template probably is coated with TiN phase and the Si$_3$N$_4$ ceramic matrix, which protect the carbon matrix against ammonia. As shown in Figure 51, it can be clearly seen the crystallization of Si$_3$N$_4$ along with TiN nanocrystals, which is more accentuated than sample pyrolyzed in nitrogen (Figure 50). The mNCHTi2.5@1400NH$_3$ sample contains crystallized phase with d-spacing of 0.38 and 0.26 nm that corresponds to (110) crystallographic planes of α-Si$_3$N$_4$ (blue lines) and TiN (red lines), respectively. The HRTEM micrograph also reveal that they are mainly composed of well-distributed graphitic structure (green arrows).

For both heat-treatment, the HRTEM images of mesoporous polytitanosilazanes derived ceramics present more crystalline regions than powders samples. As previously discussed, this difference can be attributed to the enhancement of the SSA and then increase of the interaction during pyrolysis of the material, which start to crystallize at lower temperatures (GAO *et al*., 2012). These results corroborate with XRD analysis, that show the thermal stability of polysilazanes derived ceramics is strongly affected by the design and processing route. The HRTEM results are in agreement with XRD, Raman and SEM analyses.

To obtain a better visualization of crystalline TiN phase, HRTEM micrograph (Figure 52) illustrate a single TiN nanoparticle of size about 10 nm which it is attributed the crystalline lattice fringes with lattice spacing of 0.25 nm (red lines) which matches to the inter planer spacing of (111) lattice plane.

Figure 51 – HRTEM micrograph of mNCHTi2.5@1400NH$_3$ sample.
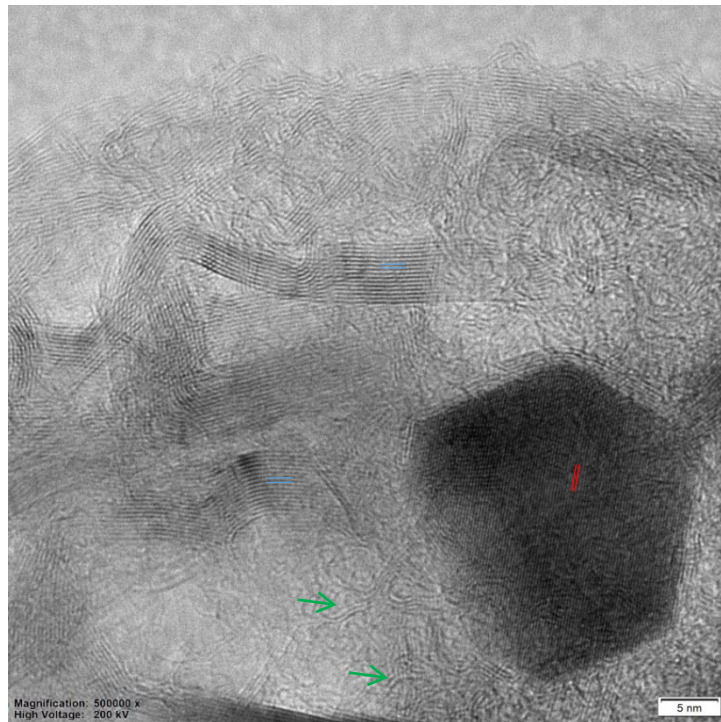
Source: Author

Figure 52 – HRTEM micrograph showing the TiN nanocrystallite.
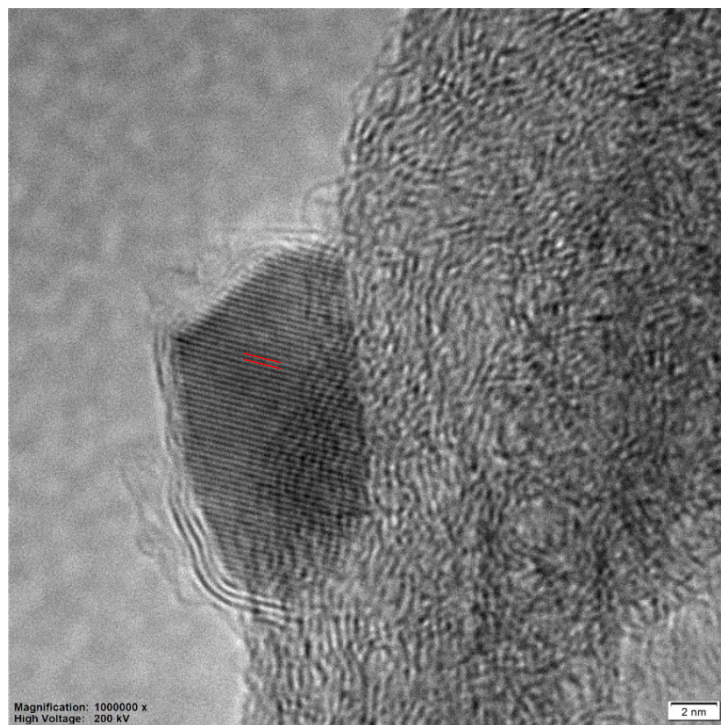
Source: Author

4.7 TEST AS ELECTRODES FOR SUPERCAPACITORS

The electrochemical performance HTT1800-derived amorphous $SiCN/Si_3N_4$ ceramics with nanoscaled TiN supported on activated carbon monoliths was analysed as an electrode for supercapacitors in a three-electrode setup to investigate its EDL capacitance in aq. 1M Na_2SO_4 as supporting electrolyte. Table 4 shows the electrochemical performance of various supercapacitors fabricated in this work.

The mesoporous 3D nanostructure shows synergistic effect of the ceramic matrix and ACM materials. Such materials have higher capacitance than pure ACM and Si-C-N-Ti ceramics, suggesting interaction between the compounds.

This remarkable characteristic is attributed unique 3D hierarchical micro/mesoporous structure of these carbon monoliths with high SSA and pore volume, which promote the fast diffusion of the reactants, ions and electrons, thus significantly improving their electrocatalytic activity and leading to fast reaction kinetics (WANG *et al.*, 2017).

The supercapacitor materials improve their capacitive performance and diffusion efficiency as electrodes. For instance, with the exception of the mNCHTi1.0@1400N$_2$ sample, the electrodes show better values of specific capacitance than pure ACM. The mNCHTi2.5@1000NH$_3$ sample provides the highest specific mass capacitances of 278 $F.g^{-1}$ and mNCHTi2.5@1400NH$_3$ sample exhibits the highest areal capacitance of 520 $F.cm^{-2}$. As compared, the ACM sample only shows a specific and areal capacitance of 102 $F.g^{-1}$ and 287 $F.cm^{-2}$, respectively (Table 4).

The basis for this PDC approach comes from the synthesis of a nanocomposite precursor through reaction of a low molecular weight Ti-based compounds with a polysilazane. TiN has been reported as an excellent electrocatalyst because of its unique electron structures, high electrical conductivity and thermal stability (WANG; WILKINSON; ZHANG, 2011). However, although samples synthesized with ratio of 1.0 has higher amount of TiN nanocrystal, samples obtained for the system using a ratio of 2.5 presents, in general, better values of capacitance. This result could be explained by the inferior chemical stability of TiN in harsh environments, such as in acidic medium used in the electrocatalysis analysis (WANG; WILKINSON; ZHANG, 2011). For this reason, the TiN phase is more effectively protected against corrosion in samples

containing a higher amount of the chemically stable Si-C-N phases, but still with a suitable amount of nanoscaled TiN, which leads to excellent capacitance performance.

In addition, the performance of electrodes pyrolyzed under ammonia is significantly greater in samples heat-treated under nitrogen, confirming the interest of nitride for catalytic activity. Although silicon carbo-nitride ceramics presents good potentials as electrodes, silicon-based nitride ceramics are the most appropriate candidates for protecting TiN and being used as electrodes for supercapacitor applications.

Table 4 – Electrochemical performance of various supercapacitors fabricated based on Ti modified HTT1800-derived amorphous SiCN/Si$_3$N$_4$ ceramics supported on activated carbon monoliths.

Sample	Specific capacitance (F g^{-1})	Areal capacitance (mF cm^{-2})
mNCHTi2.5@1400NH$_3$	260	520
mNCHTi2.5@1400N$_2$	240	480
mNCHTi2.5@1000NH$_3$	278	333
mNCHTi2.5@1000N$_2$	173	347
mNCHTi1.0@1400NH$_3$	228	91
mNCHTi1.0@1400N$_2$	36	99
mNCHTi1.0@1000NH$_3$	181	433
mNCHTi1.0@1000N$_2$	150	300
ACM	102	287

Source: Author

Considering that the highest specific and areal capacitance are obtained, we further investigated its CV in order to characterize the electrochemical capacitance, as shown in Figure 53 and 54. The shape of the CV curves reveals that it is the double layer capacitance that predominates for the mesoporous ceramics. Interestingly, the difference between both samples is the pyrolysis temperature; 1400 and 1000 for aerial and specific capacitance, respectively.

First, the mNCHTi2.5@1400NH$_3$ electrode shows a typical quasi-rectangular shape indicating good capacitive behaviour and reversibility. It is also noticeable that

CV shape increases with increasing the scan rate, which suggests a fast diffusion-controlled electrolyte ion transport kinetic on the interface (Figure 53).

In comparison with the mNCHTi2.5@1400NH$_3$, a large deviation from the rectangular shape is observed in the case of the mNCHTi2.5@1000NH$_3$ electrodes (Figure 54). The deviation from rectangularity of CVs becomes understandable at higher scan rate, probably due to the limitation in charge transfer processes that possibly results from the narrow mesoporous which will not have enough time for reaction on the surface of the electrode (SHAYEH *et al.*, 2015). BET results corroborates with this hypothesis as mNCHTi2.5@1000NH$_3$ sample exhibits the highest specific surface area (1244 m^2.g^{-1}) (Table 4).

Figure 53 – CV curves at different scan rates for mNCHTi2.5@1400NH$_3$ electrodes
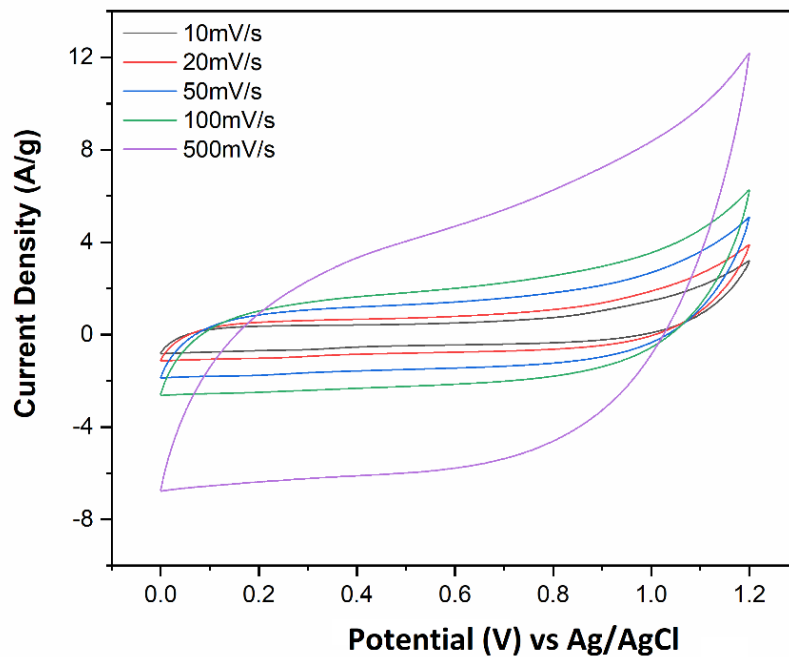
Source: Author

Figure 54 – CV curves at different scan rates for mNCHTi2.5@1000NH$_3$ electrodes.
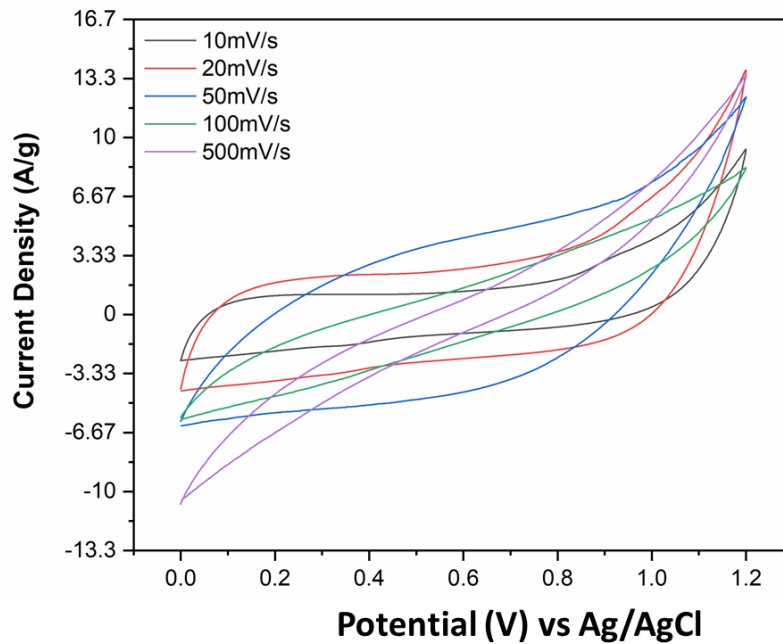
Source: Author

In order to investigate the rate capability of Si$_3$N$_4$ with nanoscaled TiN ceramics supported on ACM, the materials were further tested with different scan rates. Figures 55 and 56 show the specific and areal capacitance of the mNCHTi2.5@1000NH$_3$ and mNCHTi2.5@1400NH$_3$ with different scan rates, respectively. Although higher values of capacitance is obtained in this study, the specific capacitance of mesoporous ceramics decreased with increasing scan rate. These results suggest that the specific capacitance of the electrode significantly depends on the scan rate.

It can be observed that both specific and areal capacitance decreases with increase in the scan rate. The lower specific capacitance at higher scan rate may be attributed to the insufficient access with the resistances and circuitous diffusion pathways of ions on the electrode surface whereas at lower scan rate the ions approach the outer and inner pore surfaces, increasing the capacitance (JUSTIN; RANGA RAO, 2010; MUJAWAR *et al*., 2011).

Figure 55 – Variations in the specific capacitance versus scan rate for sample mNCHTi2.5@1000NH3.
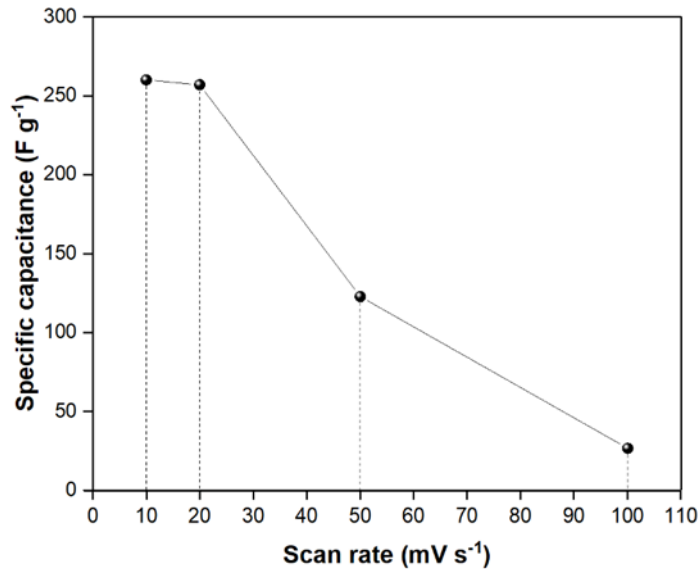
Based on these results, it can be stated that the electrochemical capacitance is strongly influenced by its pyrolysis temperature. Cordelair and Greil (2000) observed the increase electrical conductivity with the increase of pyrolysis temperature due to the establishment of percolation networks of carbon phases. Besides that, the high capacitance values at higher temperatures may be provided by the higher thermal stability of the amorphous silicon nitride matrix protecting the decomposition of the titanium nitride as well as the increase of the free carbon phase organization and presence of turbostratic carbon and graphitic-like structure. In addition, as observed in XRD and TEM analyses, the presence of TiN nanocrystallites at 1400 °C can contribute to increase the electrochemical capacitance.

Figure 56 – Variations in the aerial capacitance versus scan rate for sample mNCHTi2.5@1400NH$_3$.
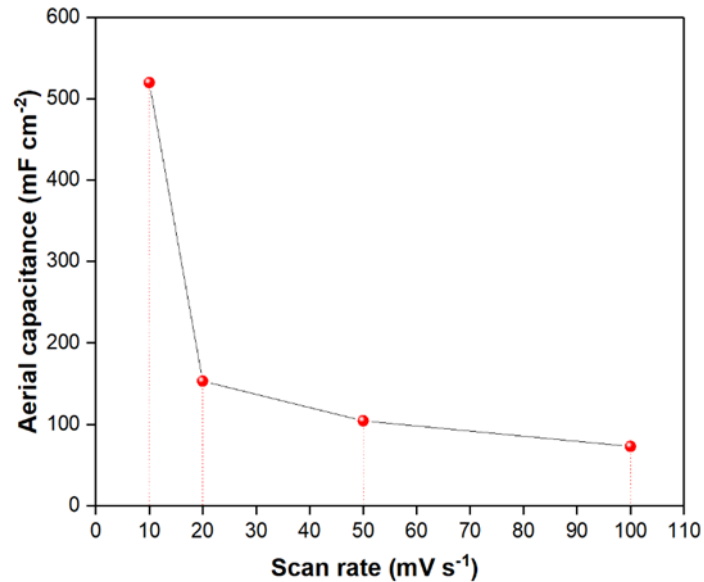
Source: Author

Moreover, heat-treatment in ammonia leads to an increase in nitrogen content. As seen in EDS analysis, sample mNCHTi2.5@1400NH$_3$ has high amount of nitrogen. The high amount of nitrogen can improve the wettability and thus increase the surface utilization of the carbon materials in the electrolyte and thereby enhance the mass transfer efficiency (WANG *et al*., 2017). Still, the presence of N-functional groups contribute to the high capacitance by enhancing the formation of the electrical double layer and its interaction with the anions in the electrolyte (ORNELAS *et al*., 2014).

Likewise, the increment of pyrolysis treatment process also is related to the formation of nanowires. Because of its one dimensional structure, the presence of these nanowires on the 3D porous ceramic matrix could led to an increase in electrical conductivity, which can influence the supercapacitor performance (WANG *et al*., 2014; XIA *et al*., 2011, 2014).

Only few papers report the use of PDC to compose electrode materials for supercapacitors. As far as we know, the specific capacitance exhibit in this work is the highest reported performances on electrodes materials based on non-oxide PDCs.

However, other electrochemical characterizations are still necessary to perform in order to obtain more information.

According to these results, supercapacitors based on HTT1800-derived amorphous Si_3N_4 ceramics with nanoscaled TiN supported on activated carbon monoliths exhibits excellent supercapacitor performance, which indicates a promising material for energy storage applications. The excellent electrochemical of the nanocomposites for supercapacitors can be attributed to the individual properties and to the synergistic effects of various factors, such as:

i) The smaller size and well distribution of the TiN nanocomposites provides an effective pathway in terms of metallic conductivity, leading to a high electrocatalytic activity

ii) The carbon matrix with a highly mesoporous nature, which facilitates accessibility of electrolyte and decrease the diffusion resistance.

iii) The Si-C-N ceramic that protect the electrode in harsh environments and avoid the electrochemical corrosion.

5 CONCLUSIONS

In this work, polytitanosilazanes were synthesized by reaction between commercially polysilazanes HTT1800 and a low molecular Ti precursor (TDMAT), with a Si:Ti molar ratio of 2.5 and 1.0. FTIR and NMR analysis confirmed the interaction of both compounds during the sythesis, mostly through the reaction between Si-H units from HTT1800 with the NCH_3 groups from TDMAT..

The as-obtained polytitanosilzanes were pyrolyzed in nitrogen and ammonia. Structural evolution of polytitanosilazanes during pyrolysis was studied using TGA, FTIR and NMR. The results suggested the occurrence of mainly dehydrocoupling and transamination reactions during pyrolysis and, in the case of ammonia, the free carbon removal.

Powders threated in nitrogen lead to nanocomposites of a TiC_xN_{1-y} nanophase embedded in an amorphous SiCN matrix. XRD and TEM analyses revealed an amourphous SiCN ceramic matrix amorphous, since no crystallites related to silicon carbide or silicon nitride were detected up to 1500 °C. This indicates that the presence of nanocrystalline phases have a major influence on crystallization of SiCN matrix under nitrogen, which can delay or avoid the crystallization of SiCN ceramics

In the case of the powders threated in ammonia, the heat-treatment led to TiN nanocrystals in a Si_3N_4 ceramic matrix. XRD analysis confirmed that the polytitanosilazanes derived ceramics were structurally amorphous until 1400 °C. At 1500 °C, small Si_3N_4 crystalline phases were detected and the size of TiN nanocrystals slightly increased.

The as-synthesized polytitanosilazanes were successfully impregnated by nanocasting method using an activated carbon monolith as template and subsequently pyrolyzed in ammonia and nitrogen. After pyrolysis, micro/mesoporous structures have been obtained. By varying the type of gas and pyrolysis temperature, the pore structure and SSA can be adjusted. The results of Raman showed a high degree of disorder of polymer-derived ceramic monoliths, corroborating with XRD results. Moreover, TEM images confirmed the presence of amorphous and graphitic-like structure, TiN and

Si_3N_4 nanocrystallites in the pyrolyzed samples at 1400 °C under ammonia and nitrogen.

The polytitanosilazanes derived ceramics presented characteristics that enable their use as electrodes. The presence of the polymer-derived-ceramic matrix may protect the electrode against harsh environments and avoid the electrochemical corrosion. Also, the small size and well distribution of TiN nanocrystallites provides an effective pathway in terms of metallic conductivity, leading to a high electrocatalytic activity. In addition, the highly mesoporous 3D nanostructure shows an excellent electrochemical performance as they enable accessibility of electrolyte and decrease the diffusion resistance. The mesoporous polytitanosilazanes derived ceramics with Si:Ti ratio of 2.5 and threated under ammonia exhibited the highest values of capacitance as electrode materials for supercapacitors applications. To the best of our knowledge, this work reported the highest specific capacitance using electrodes materials based on non-oxide PDCs.

In conclusion, mesoporous TiN/Si_3N_4 and TiN/SiCN nanocomposites prepared by nanocasting method showed good capacitance properties, which indicates they are a promising material for energy storage applications. The remarkable capacitance properties of this material are attributed to the synergistic effects between the conductive activated carbon monolith and the catalytic activity of Ti modified Si_3N_4/SiCN ceramics.

5.1 FUTURE PERSPECTIVES

Additional characterizations of the mesoporous ceramics should be proceeded to ensure that the electrochemical properties can be reproduced and compared with other materials that are currently available. As future works would be also interesting to impregnate the polytitanosilazanes into other types of porous carbon materials in order to achieve higher energy densities. Furthermore, since the results that we obtained are very encouraging, the mesoporous ceramics should be further applied on other energy storage systems.

REFERENCES

ABASS, M. A. et al. Synthesis and electrochemical performance of a polymer-derived silicon oxycarbide/boron nitride nanotube composite. **RSC Advances**, v. 7, p. 21576–21584, 2017.

AINGER, F. W.; HERBERT, J. M. The Preparation of Phosphorous-Nitrogen Compunds as Non-porous Solids. In: POPPER, P. (Ed.). . **Special Ceramics**. New York: Academic Press, 1960. p. 168–182.

ARMAND, M.; TARASCON, J.-M. Building better batteries. **Nature**, v. 451, n. 7179, p. 652–657, 2008.

BAHLOUL, D. et al. Preparation of Silicon Carbonitrides from an Organosilicon Polymer: I, Thermal Decomposition of the Cross-linked Polysilazane. **Journal of the American Ceramic Society**, v. 76, n. 5, p. 1156–1162, 1993.

BARROSO, G. et al. Polymeric and ceramic silicon-based coatings-a review. **Journal of Materials Chemistry A**, v. 7, n. 5, p. 1936–1963, 2019.

BARSHILIA, H. C.; RAJAM, K. S. Raman spectroscopy studies on the thermal stability of TiN, CrN, TiAlN coatings and nanolayered TiN/CrN, TiAlN/CrN multilayer coatings. **Journal of Materials Research**, v. 19, n. 11, p. 3196–3205, 2004.

BECHELANY, M. C. et al. In Situ Controlled Growth of Titanium Nitride in Amorphous Silicon Nitride : A General Route Toward Bulk Nitride Nanocomposites with Very High Hardness. **Advanced Materials**, v. 26, p. 6548–6553, 2014.

BECHELANY, M. C. et al. Nanocomposites through the Chemistry of Single-Source Precursors: Understanding the Role of Chemistry behind the Design of Monolith-Type Nanostructured Titanium Nitride/Silicon Nitride. **Chemistry - A European Journal**, v. 23, n. 4, p. 832–845, 2017.

BELLINI, C. et al. Tailored Cyclic and Linear Polycarbosilazanes by Barium-Catalyzed N-H/H-Si Dehydrocoupling Reactions. **Angewandte Chemie - International Edition**, v. 55, n. 11, p. 3744–3748, 2016.

BERCKMANS, G. et al. Cost projection of state of the art lithium-ion batteries for electric vehicles up to 2030. **Energies**, v. 10, n. 9, 2017.

BERNARDO, E. et al. Advanced ceramics from preceramic polymers modified at the nano-scale: A review. **Materials**, v. 7, n. 3, p. 1927–1956, 2014.

BHANDAVAT, R.; PEI, Z.; SINGH, G. Polymer-derived ceramics as anode material for rechargeable Li-ion batteries: a review. **Nanomaterials and Energy**, v. 1, p. 324–

337, 2012.

BIASETTO, L. et al. Polymer-derived microcellular SiOC foams with magnetic functionality. **Journal of Materials Science**, v. 43, n. 12, p. 4119–4126, 2008.

BORCHARDT, L. et al. Preparation and application of cellular and nanoporous carbides. **Chemical Society Reviews**, v. 41, n. 15, p. 5053–5067, 2012.

BORDIA, R. K.; RAJ, R. Sintering Behavior of Ceramic Films Constrained by a Rigid Substrate. **Journal of the American Ceramic Society**, v. 68, n. 6, p. 287–292, 1985.

BRINCKMANN, S. A. et al. Stereolithography of SiOC Polymer-Derived Ceramics Filled with SiC Micronwhiskers. **Advanced Engineering Materials**, v. 20, n. 11, p. 1–10, 2018.

BURNS, G. T.; CHANDRA, G. Pyrolysis of Preceramic Polymers in Ammonia: Preparation of Silicon Nitride Powders. **Journal of the American Ceramic Society**, v. 72, n. 2, p. 333–337, 1989.

CAO, Z.; WEI, B. A perspective: Carbon nanotube macro-films for energy storage. **Energy and Environmental Science**, v. 6, n. 11, p. 3183–3201, 2013.

CARRETTE, B. L.; FRIEDRICH, K. A.; STIMMING, U. Fuel Cells - Fundamentals and Applications. **Fuel Cells**, v. 1, n. 1, p. 5–39, 2001.

CHANTRELL, P. G.; POPPER, P. Inorganic Polymers and Ceramics. In: POPPER, P. (Ed.). . **Special Ceramics**. New York: Academic Press, 1965. p. 87–103.

CHAVEZ, R. et al. Effect of Ambient Atmosphere on Crosslinking of Polysilazanes. **Journal of Applied Polymer Science**, v. 119, p. 794–802, 2011.

CHEN, Y. et al. Quantitative study on structural evolutions and associated energetics in polysilazane-derived amorphous silicon carbonitride ceramics. **Acta Materialia**, v. 72, p. 22–31, 2014.

CHENG, Y. H. et al. Substrate bias dependence of Raman spectra for TiN films deposited by filtered cathodic vacuum arc Substrate bias dependence of Raman spectra for TiN films deposited by filtered cathodic vacuum arc. **Journal of Applied Physics**, v. 92, n. 4, p. 1845–1849, 2002.

CHRISTEN, T.; CARLEN, M. W. Theory of ragone plots. **Journal of Power Sources**, v. 91, n. 2, p. 210–216, 2000.

COAN, T. et al. A novel organic-inorganic PMMA/polysilazane hybrid polymer for corrosion protection. **Progress in Organic Coatings**, v. 89, p. 220–230, 2015.

COLOMBO, P. et al. Polymer-derived ceramics: 40 Years of research and innovation in advanced ceramics. **Journal of the American Ceramic Society**, v. 93, n. 7, p.

1805–1837, 2010.

CORDELAIR, J.; GREIL, P. Electrical conductivity measurements as a microprobe for structure transitions in polysiloxane derived Si-O-C ceramics. **Journal of the European Ceramic Society**, v. 20, n. 12, p. 1947–1957, 2000.

DANKO, G. A. et al. Comparison of Microwave Hybrid and Conventional Heating of Preceramic Polymers to Form Silicon Carbide and Silicon Oxycarbide Ceramics. **Journal of the American Ceramic Society**, v. 83, n. 7, p. 1617–1625, 2000.

DAVID, L. et al. Three-dimensional polymer-derived ceramic/graphene paper as a Li-ion battery and supercapacitor electrode. **RSC Advances**, v. 6, n. 59, p. 53894–53902, 2016.

DECKWERTH, M.; RÜSSEL, C. A new polymeric route to silicon carbide and silicon nitride using elementary silicon as starting material. **Journal of Materials Science**, v. 29, n. 17, p. 4500–4504, 1994.

DEMIRBAS, A. Global renewable energy projections. **Energy Sources, Part B: Economics, Planning and Policy**, v. 4, n. 2, p. 212–224, 2009.

DICKS, A. The Role of Carbon in Fuel Cells. **Journal of Power Sources**, n. 156, p. 128–141, 2006.

DODDS, P. E. et al. Hydrogen and fuel cell technologies for heating: A review. **International Journal of Hydrogen Energy**, v. 40, n. 5, p. 2065–2083, 2015.

DONG, S.; ZHAO, T.; XU, C. Synthesis and Thermal Behavior of Polymeric Precursors for S-B-C-N Ceramic. **Journal of Applied Polymer Science**, v. 118, p. 3400–3406, 2010.

FERRARI, A. C.; ROBERTSON, J. Raman spectroscopy of amorphous , nanostructured , diamond − like carbon , and nanodiamond. **The Royal Society**, v. 362, p. 2477–2512, 2004.

FLORES, O. et al. Selective cross-linking of oligosilazanes to tailored meltable polysilazanes for the processing of ceramic SiCN fibres. **Journal of Materials Chemistry A**, v. 1, p. 15406–15415, 2013.

FONBLANC, D. et al. Crosslinking chemistry of poly(vinylmethyl-co-methyl)silazanes toward low-temperature formable preceramic polymers as precursors of functional aluminium-modified Si-C-N ceramics. **Dalton Transactions**, v. 47, n. 41, p. 14580–14593, 2018.

GAO, Y. et al. Processing route dramatically influencing the nanostructure of carbon-rich SiCN and SiBCN polymer-derived ceramics. Part I: Low temperature thermal

transformation. **Journal of the European Ceramic Society**, v. 32, n. 9, p. 1857–1866, 2012.

GONZÁLEZ, A. et al. Review on supercapacitors: Technologies and materials. **Renewable and Sustainable Energy Reviews**, v. 58, p. 1189–1206, 2016.

GRACZYK-ZAJAC, M. et al. Electrochemical studies of carbon-rich polymer-derived SiCN ceramics as anode materials for lithium-ion batteries. **Journal of the European Ceramic Society**, v. 30, n. 15, p. 3235–3243, 2010.

GRACZYK-ZAJAC, M. et al. New Insights into Understanding Irreversible and Reversible Lithium Storage within SiOC and SiCN Ceramics. **Nanomaterials**, v. 5, n. 1, p. 233–245, 2015.

GRACZYK-ZAJAC, M.; FASEL, C.; RIEDEL, R. Polymer-derived-SiCN ceramic/graphite composite as anode material with enhanced rate capability for lithium ion batteries. **Journal of Power Sources**, v. 196, n. 15, p. 6412–6418, 2011.

GREIL, P. Active-filler-controlled Pyrolysis of Preceramic Polymers. **Journal of the American Ceramic Society1**, v. 78, n. 4, p. 835–848, 1995.

GUOPING, W. et al. A modified graphite anode with high initial efficiency and excellent cycle life expectation. **Solid State Ionics**, v. 176, n. 9–10, p. 905–909, 2005.

HAILE, S. M. Fuel cell materials and components ✣. **Acta Materialia**, v. 51, p. 5981–6000, 2003.

HALIM, M. et al. Pseudocapacitive Characteristics of Low-Carbon Silicon Oxycarbide for Lithium-Ion Capacitors. **ACS Applied Materials and Interfaces**, v. 9, n. 24, p. 20566–20576, 2017.

IONESCU, E. et al. Phase separation of a hafnium alkoxide-modified polysilazane upon polymer-to-ceramic transformation-A case study. **Journal of the European Ceramic Society**, v. 32, n. 9, p. 1873–1881, 2012.

IONESCU, E.; KLEEBE, H. J.; RIEDEL, R. Silicon-containing polymer-derived ceramic nanocomposites (PDC-NCs): Preparative approaches and properties. **Chemical Society Reviews**, v. 41, n. 15, p. 5032–5052, 2012.

IRO, Z. S.; SUBRAMANI, C.; DASH, S. S. A brief review on electrode materials for supercapacitor. **International Journal of Electrochemical Science**, v. 11, n. 12, p. 10628–10643, 2016.

JUSTIN, P.; RANGA RAO, G. CoS spheres for high-rate electrochemical capacitive energy storage application. **International Journal of Hydrogen Energy**, v. 35, n. 18, p. 9709–9715, 2010.

KIM, B. K. et al. **Electrochemical Supercapacitors for Energy Storage and**

Conversion. [s.l: s.n.].

KOLATHODI, M. S. et al. Polysiloxane-functionalized graphene oxide paper: Pyrolysis and performance as a Li-ion battery and supercapacitor electrode. **RSC Advances**, v. 6, n. 78, p. 74323–74331, 2016.

KORENBLIT, Y. et al. High-Rate Electrochemical Capacitors Based on Ordered Mesoporous Silicon Carbide-Derived Carbon. **ACS Nano**, v. 4, n. 3, p. 1337–1344, 2010.

KRAYTSBERG, A.; EIN-ELI, Y. Review A Review of Advanced Materials for Proton Exchange Membrane Fuel Cells. **Energy & Fuels**, v. 28, n. 12, p. 7303–7330, 2014.

KROKE, E. et al. Silazane derived ceramics and related materials. **Materials Science and Engineering: R: Reports**, v. 26, n. 4–6, p. 97–199, 2002.

KRÜNER, B. et al. Carbide-derived carbon beads with tunable nanopores from continuously produced polysilsesquioxanes for supercapacitor electrodes. **Sustainable Energy and Fuels**, v. 1, n. 7, p. 1588–1600, 2017.

LALE, A. et al. Organosilicon polymer-derived mesoporous 3D silicon carbide, carbonitride and nitride structures as platinum supports for hydrogen generation by hydrolysis of sodium borohydride. **International Journal of Hydrogen Energy**, v. 41, n. 34, p. 15477–15488, 2016.

LALE, A. et al. A comprehensive study on the influence of the polyorganosilazane chemistry and material shape on the high temperature behavior of titanium nitride/silicon nitride nanocomposites. **Journal of the European Ceramic Society**, p. 1–9, 2017.

LALE, A. et al. Polymer-Derived Ceramics with engineered mesoporosity: From design to application in catalysis. **Surface and Coatings Technology**, v. 350, n. May, p. 569–586, 2018.

LIBICH, J. et al. Supercapacitors: Properties and applications. **Journal of Energy Storage**, v. 17, n. March, p. 224–227, 2018.

LIQUN, D. et al. Fabrication and electrochemical performance of nanoporous carbon derived from silicon oxycarbide. **Microporous and Mesoporous Materials**, v. 202, n. C, p. 97–105, 2015.

LIU, H. J. et al. Ordered hierarchical mesoporous/microporous carbon derived from mesoporous titanium-carbide/carbon composites and its electrochemical performance in supercapacitor. **Advanced Energy Materials**, v. 1, n. 6, p. 1101–1108, 2011.

LÜCKE, J. et al. Synthesis and Characterization of Silazane-Based Polymers as Precursors for Ceramic Matrix Composites. **Applied Organometallic Chemistry**, v. 11, n. 2, p. 181–194, 1997.

MATHIS, T. S. et al. Energy Storage Data Reporting in Perspective—Guidelines for Interpreting the Performance of Electrochemical Energy Storage Systems. **Advanced Energy Materials**, v. 9, n. 39, p. 1–13, 2019.

MEIER, A. et al. Silicon oxycarbide-derived carbons from a polyphenylsilsequioxane precursor for supercapacitor applications. **Microporous and Mesoporous Materials**, v. 188, p. 140–148, 2014.

MERA, G. et al. Carbon-rich SiCN ceramics derived from phenyl-containing poly (silylcarbodiimides). **Journal of the European Ceramic Society**, v. 29, p. 2873–2883, 2009.

MERA, G. et al. Ceramic Nanocomposites from Tailor-Made Preceramic Polymers. **Nanomaterials**, v. 5, n. 2, p. 468–540, 2015.

MOURDIKOUDIS, S.; LIZ-MARZÁN, L. M. Oleylamine in nanoparticle synthesis. **Chemistry of Materials**, v. 25, n. 9, p. 1465–1476, 2013.

MUJAWAR, S. H. et al. Electropolymerization of polyaniline on titanium oxide nanotubes for supercapacitor application. **Electrochimica Acta**, v. 56, n. 12, p. 4462–4466, 2011.

MUKHERJEE, S.; REN, Z.; SINGH, G. Molecular polymer-derived ceramics for applications in electrochemical energy storage devices. **Journal of Physics D: Applied Physics**, v. 51, n. 46, 2018.

NEJAT, P. et al. A global review of energy consumption, CO2 emissions and policy in the residential sector (with an overview of the top ten CO2 emitting countries). **Renewable and Sustainable Energy Reviews**, v. 43, p. 843–862, 2015.

OMER, A. M. Sustainable development and environmentally friendly energy systems in sudan. **International Journal of Physical Sciences and Engineering**, v. 1, n. 1, p. 1–39, 2017.

ORNELAS, O. et al. On the origin of the high capacitance of nitrogen-containing carbon nanotubes in acidic and alkaline electrolytes †. **Chem. Commun.**, v. 50, p. 11343–11346, 2014.

PAYMAN, A.; PIERFEDERICI, S.; MEIBODY-TABAR, F. Energy control of supercapacitor/fuel cell hybrid power source. **Energy Conversion and Management**, v. 49, n. 6, p. 1637–1644, 2008.

PROUST, V. et al. Polymer-derived Si-C-Ti systems: From titanium nanoparticle-filled polycarbosilanes to dense monolithic multi-phase components with high hardness. **Journal of the European Ceramic Society**, v. 36, n. 15, p. 3671–3679, 2016.

RIBEIRO, L. F. B. et al. A novel PAN/silazane hybrid polymer for processing of carbon-based fibres with extraordinary oxidation resistance. **Journal of Materials Chemistry A**, v. 5, p. 720–729, 2016.

SAHAY, K.; DWIVEDI, B. Supercapacitors energy storage system for power quality improvement: An overview. **Journal of Electrical Systems**, v. 5, n. 4, 2009.

SATO, K. et al. Low Temperature Crystallization Behavior of α-Si3N4 from Ti-Doped Amorphous Silicon Nitride Derived from Polytitanasilazanes. **Journal of the Ceramic Society of Japan**, v. 114, n. 1330, p. 502–506, 2006.

SHAFEEYAN, M. S. et al. Ammonia modification of activated carbon to enhance carbon dioxide adsorption: Effect of pre-oxidation. **Applied Surface Science**, v. 257, n. 9, p. 3936–3942, 2011.

SHAH, S. R.; RAJ, R. Mechanical properties of a fully dense polymer derived ceramic made by a novel pressure casting process. **Acta Materialia**, v. 50, n. 16, p. 4093–4103, 2002.

SHAO-HORN, Y. et al. Instability of Supported Platinum Nanoparticles in Low-Temperature Fuel Cells. **Topics in Catalysis**, v. 46, p. 285–305, 2007.

SHAYEH, J. S. et al. Physioelectrochemical investigation of the supercapacitive performance of a ternary nanocomposite by common electrochemical methods and fast Fourier transform voltammetry. **New Journal of Chemistry**, v. 39, n. 12, p. 9454–9460, 2015.

SHRIVER, D. F.; DREZDZON, M. A. **The Manipulation of Air-Sensitive Compounds**. 2nd. ed. New York: [s.n.].

SING, K. S. W. et al. Reporting Physisorption Data for Gas/Solid Systems with Special Reference to the Determination of Surface Area and Porosity. **Pure and Applied Chemistry**, v. 57, p. 603–619, 1985.

SING, K. S. W.; WILLIAMS, R. T. Physisorption Hysteresis Loops and the Characterization of Nanoporous Materials. **Adsorption Science & Technology**, v. 22, n. 10, p. 773–782, 2004.

SONG, Y. C.; ZHAO, C. X.; LU, Y. Synthesis and pyrolysis of polysilazane as the precursor of Si3N4/SiC ceramic. **Journal of Materials Science**, v. 29, p. 5745–5756, 1994.

SUZUKI, M. et al. Synthesis of Silicon Carbide-Silicon Nitride Composite Ultrafine Particles Using a Carbon Dioxide Laser. **Journal of the American Ceramic Society**, v. 76, n. 5, p. 1195–1200, 1993.

SWAIN, I. P.; PATI, S.; BEHERA, S. K. A preceramic polymer derived nanoporous carbon hybrid for supercapacitors. v. 55, p. 8631–8634, 2019.

TAMURA, K. et al. MEGA6: Molecular evolutionary genetics analysis version 6.0. **Molecular Biology and Evolution**, v. 30, n. 12, p. 2725–2729, 2013.

TOLOSA, A. et al. Electrospinning and electrospraying of silicon oxycarbide-derived nanoporous carbon for supercapacitor electrodes. **Journal of Power Sources**, v. 313, p. 178–188, 2016.

VERBEEK, W.; WINTER, G. **Formkorper aus Siliciucarbid und Verfahren zu uhrer Herstellung**German, 1974.

WANG, K. et al. Conducting Polymer Nanowire Arrays for High Performance Supercapacitors. **Small**, n. 1, p. 14–31, 2014.

WANG, Y.-J.; WILKINSON, D. P.; ZHANG, J. Noncarbon Support Materials for Polymer Electrolyte Membrane Fuel Cell Electrocatalysts. **Chemical Reviews**, v. 111, n. 12, p. 7625–7651, 2011.

WANG, Y. et al. A review of polymer electrolyte membrane fuel cells : Technology , applications , and needs on fundamental research. **Applied Energy**, v. 88, n. 4, p. 981–1007, 2011.

WANG, Y. et al. Nitrogen-doped porous carbon monoliths from polyacrylonitrile (PAN) and carbon nanotubes as electrodes for supercapacitors. **Nature Publishing Group**, n. September 2016, p. 1–11, 2017.

WILAMOWSKA, M.; GRACZYK-ZAJAC, M.; RIEDEL, R. Composite materials based on polymer-derived SiCN ceramic and disordered hard carbons as anodes for lithium-ion batteries. **Journal of Power Sources**, v. 244, p. 80–86, 2013.

WINTER, M.; BRODD, R. J. What are batteries, fuel cells, and supercapacitors? **Chemical reviews**, v. 104, n. 10, p. 4245–69, 2004.

WU, Y. P. et al. Effects of pretreatment of natural graphite by oxidative solutions on its electrochemical performance as anode material. **Electrochimica Acta**, v. 48, n. 7, p. 867–874, 2003.

XIA, X. et al. Self-supported hydrothermal synthesized hollow Co3O4 nanowire arrays with high supercapacitor capacitance. **Chem, J Mater**, v. 21, p. 9319–9325, 2011.

XIA, X. et al. A New Type of Porous Graphite Foams and Their Integrated Composites with Oxide/Polymer Core/Shell Nanowires for Supercapacitors: Structural Design, Fabrication, and Full Supercapacitor Demonstrations. **Nano letters**, v. 14, p. 1651–1658, 2014.

XIE, Y. et al. Review of Research on Template Methods in Preparation of Nanomaterials. **Journal of Nanomaterials**, v. 2016, p. 1–10, 2016.

YANG, J. et al. Optimized mesopores enabling enhanced rate performance in novel ultrahigh surface area meso-/microporous carbon for supercapacitors. **Nano Energy**, v. 33, n. December 2016, p. 453–461, 2017.

YIVE, N. S. C. K. et al. Thermogravimetric Analysis/Mass Spectrometry Investigation of the Thermal Conversion of Organosilicon Precursors into Ceramics under Argon and Ammonia. 2. Poly(silazanes). **Chemistry of Materials**, v. 4, n. 6, p. 1263–1271, 1992.

ZHANG, W. et al. Recent development of carbon electrode materials and their bioanalytical and environmental applications. **Chemical Society Reviews**, v. 45, n. 3, p. 715–752, 2016.

ZHAO, H. et al. Review of energy storage system for wind power integration support. **Applied Energy**, v. 137, p. 545–553, 2015.